

# RotCurves: A PYTHON package for efficient modelling and fitting of galactic rotation curves at high-z

A. Nestor Shachar  A. Sternberg , S. H. Price , N. M. Förster Schreiber , R. Genzel , L. J. Tacconi , H. Übler  C. Barfety , A. Burkert , J. Chen , R. Davies , F. Eisenhauer , J. M. Espejo Salcedo , R. Herrera-Camus , J. B. Jolly , L. L. Lee , T. Naab , S. Pastras , C. Pulsoni , T. T. Shimizu , G. Tozzi 

<sup>1</sup>School of Physics and Astronomy, Tel Aviv University, Tel Aviv 6997801, Israel

<sup>2</sup>Center for Computational Astrophysics, Flatiron Institute, 162 5th Avenue, New York, NY, 10010, USA

<sup>3</sup>Max-Planck-Institut für Extraterrestrische Physik (MPE), Giessenbachstr.1, 85748 Garching, Germany

<sup>4</sup>Space Telescope Science Institute, 3700 San Martin Drive, Baltimore, Maryland 21218, USA

<sup>5</sup>Universitäts-Sternwarte Ludwig-Maximilians-Universität (USM), Scheinerstr. 1, München, D-81679, Germany

<sup>6</sup>Departamento de Astronomía, Universidad de Concepción, Barrio Universitario, Concepción, Chile

<sup>7</sup>Max Planck Institute for Astrophysik (MPA), Karl-Schwarzschild-Str 1, D-85748 Garching, Germany

Accepted 2026 January 11. Received 2026 January 11; in original form 2025 November 13

## ABSTRACT

Rotation curves are a fundamental tool in the study of galaxies across cosmic time, and with the advent of large integral field unit (IFU) kinematic surveys there is an increasing need for efficient and flexible modelling tools. We present `RotCurves`, a parametric forward-modeling tool designed for rotation curve analysis at high-z, correcting for “beam smearing” by projecting and convolving the beam PSF in the plane of the galaxy. We benchmark `RotCurves` against the established parametric code `dysmalpy` using synthetic observations. The typical runtime with `RotCurves` is a few  $\sim 10$ ms, a factor  $\approx 250$  faster than `dysmalpy` for a single realization. For well-resolved systems (PSF FWHM  $< R_{\text{eff}}$ ), the mock observed rotation and dispersion curves agree to within 5% up to  $3R_{\text{eff}}$ , whereas in marginally resolved systems (PSF FWHM  $\gtrsim 1.5R_{\text{eff}}$ ) discrepancies increase to up to 15%. Using a built-in MCMC fitting procedure, `RotCurves` recovers well the intrinsic model parameters across a wide range of galaxy properties and accounting for realistic noise patterns. Systematic biases emerge for the effective radius and for low disk masses ( $M_{\text{disk}} \lesssim 3 \times 10^9 M_{\odot}$ ). We show excellent parameter recovery at high signal-to-noise ratios (S/N  $\gtrsim 25$ ), with increasing deviations in parameter recovery at lower S/N. `RotCurves` is best suited for inclinations of  $10^\circ < i < 80^\circ$ . `RotCurves` is built as an exploratory tool for rapid testing of mass model assumptions, parameter studies and for efficiently processing large samples of observational data from large IFU surveys. The code is publicly available on [github](#).

**Key words:** galaxies: kinematics and dynamics – galaxies: high-redshift – galaxies: disc – Software

## 1 INTRODUCTION

Galaxy rotation curves have long been a powerful tool to study the structure and evolution of galaxies. As direct probes of the gravitational potentials, they are key for understanding galactic structure, evolution, dynamics, and the nature of the dark matter halos. Since the pioneering work of Burbidge et al. (1959); Rubin & Ford (1970); Bosma (1981); van der Kruit & Allen (1978) and many others, the study of rotation curves has evolved from single-object spectroscopy in the Local Universe to large integral field unit (IFU) surveys and millimeter interferometry of distance objects across cosmic time (Courteau 1997; Courteau & Dutton 2015; de Blok et al. 2008; Förster Schreiber et al. 2009; Wisnioski et al. 2015; Stott et al. 2016; Harrison et al. 2017; Genzel et al. 2017, 2020; Tiley et al. 2019; Bouché et al. 2022; Nestor Shachar et al. 2023; Puglisi et al. 2023; Lee et al. 2025a). Studies at higher redshifts have shown that most “main sequence” star-forming galaxies (SFGs) at redshifts  $z \sim 1 - 3$  are rotating turbulent disks (Förster Schreiber et al. 2009; Förster

Schreiber & Wuyts 2020; Wuyts et al. 2016; Genzel et al. 2017, 2020; Lang et al. 2017; Wisnioski et al. 2019; Bouché et al. 2022). Recent kinematic studies from ground-based mm interferometric and JWST IFU data indicate that the prevalence of rotating, turbulent gas disks SFGs extends out to  $z \sim 6$  (e.g. Lee et al. 2025a, and references within), with tentative evidence for rotation as early as  $z \sim 14$  (Scholtz et al. 2025). Order rotation points out to a more regulated scenario of galaxy evolution over frequent violent major-mergers. More recently, JWST/NIRCam have established that star forming galaxies are predominantly disks, with some evidence for the existence of spiral structure, up to redshifts of  $z \sim 6$  (Ferreira et al. 2023; Kartaltepe et al. 2023; Huertas-Company et al. 2024; Kuhn et al. 2024; Tohill et al. 2024; Smethurst et al. 2025; Espejo Salcedo et al. 2025b; Géron et al. 2025; Chugunov et al. 2025; van der Wel & Meidt 2025). Analysis of rotation curves is essential for the study of galaxies across cosmic time, even at the earliest stages of galaxy formation.

In this paper we present our rotation curve modeling tool `RotCurves`.

### 1.1 Spectroscopic surveys

The advent of large-scale ground-based surveys, especially with the introduction of IFU and adaptive-optics modules, has revolutionized our ability to study galaxy kinematics with unprecedented detail and statistical power. In the Local Universe, The HI Nearby Galaxy Survey (THINGS: [Walter et al. 2008](#); [de Blok et al. 2008](#)), followed by LITTLE THINGS targeting dwarf galaxies ([Hunter et al. 2012](#)), mapped the neutral hydrogen through 21cm emission with extremely high spatial ( $\sim 100$ pc) and spectral ( $\sim 5$  km s $^{-1}$ ) resolutions. In the optical, the MaNGA survey targeted an unprecedented number of  $\sim 10,000$  galaxies ([Bundy et al. 2015](#); [Abdurro'uf et al. 2022](#)), while other IFU-surveys provided a higher spatial and spectral resolutions for large samples, such as SAMI ([Croom et al. 2021](#)) and CALIFA ([Sánchez et al. 2016, 2023](#)). Subsequent studies have focused on resolving the kinematics of nearby galaxies at high spatial resolution, for example using samples from MaNGA ([Yoon et al. 2021](#)), the DISKMASS survey ([Martinsson et al. 2013](#)), the Extended Disk Galaxy Explore Science (EDGES) survey ([Richards et al. 2016](#)), the SPARC sample (175 galaxies [Lelli et al. 2016a, 2017](#)), and others ([Cappellari et al. 2013](#); [Gómez-López et al. 2019](#); [Lang et al. 2020](#); [Di Teodoro et al. 2021, 2023](#)).

At higher redshifts, the small apparent sizes of galaxies together with surface brightness dimming, which scales as  $(1+z)^4$ , are a major challenge for resolved kinematic studies of galaxies, both spatially and spectrally. Ground-based observations from large telescopes were of great importance both in the near-infrared (NIR), tracing rest-optical emission lines, and in mm-radio interferometry, with little atmospheric absorption. The SINS/zC-SINF survey of H $\alpha$  kinematics with SINFONI at the Very Large Telescope targeted  $\sim 80$  main sequence massive SFGs at  $z \sim 1.5-2.5$  in seeing-limited mode, including 35 for which very deep, high-resolution adaptive optics-assisted observations were also obtained (PSF FWHM  $\sim 0.15''$  [Förster Schreiber et al. 2009, 2018](#); [Mancini et al. 2011](#)). Other studies have increased the number of galaxies using both VLT/SINFONI ([Epinat et al. 2009](#); [Gnerucci et al. 2011](#)) and KECK/OSIRIS ([Law et al. 2009](#)), in both seeing-limited and adaptive-optics assisted modes. In other cases, the magnification caused by gravitational lensing can resolve galaxies down to the  $\sim 100$ pc scales and provide highly detailed velocity maps ([Livermore et al. 2015](#); [Leethochawalit et al. 2016](#); [Liu et al. 2023a](#)).

Multi-target IFU instruments have been invaluable in increasing statistics, targeting multiple galaxies at once. In the near-IR, the VLT/KMOS allowed large surveys to collectively target thousands of galaxies at  $z \sim 1-3$ , with surveys such as KMOS<sup>3D</sup> ( $\sim 700$  galaxies, [Wisnioski et al. 2019](#)), KROSS ( $\sim 800$  galaxies, [Stott et al. 2016](#); [Harrison et al. 2017](#)) and KGES ( $\sim 300$  galaxies, [Tiley et al. 2019, 2021](#)). Others have used KMOS to obtain deep observation on smaller samples, (e.g., KURVS, targeting 22 low mass galaxies at  $z \sim 1$ , [Puglisi et al. 2023](#)). In the optical, VLT/MUSE have been used to resolve kinematics for  $z \lesssim 1$  galaxies, such as the MUSE Hubble Ultra Deep Field ([Contini et al. 2016](#); [Guérou et al. 2017](#)) or the MXDF ([Bouché et al. 2022](#)).

In mm interferometry, ALMA and NOEMA have played a key role by tracing CO molecular gas kinematics up to  $z \sim 3$  ([Genzel et al. 2013](#); [Tacconi et al. 2013, 2018](#); [Chen et al. 2017](#); [Übler et al. 2018](#); [Tadaki et al. 2018](#); [Molina et al. 2019](#); [Rizzo et al. 2021, 2023](#); [Pastrás et al. 2025](#), [Jolly et al., in prep.](#)), most notably with the ALMA-ALPAK survey ([Rizzo et al. 2023](#)) and NOEMA<sup>3D</sup> ([Pastrás et al. 2025](#); [Jolly et al., in prep.](#)). More recently, the strong [CII] line have been used in kinematic surveys at higher redshifts  $z \sim 3-6$ , such as the ALPINE survey ([Jones et al. 2021](#)), the CRISTAL survey ([Herrera-Camus et al. 2025](#); [Lee et al. 2025a](#)), REBELS ([Rowland et al. 2024](#)) and others ([Smit et al. 2018](#); [Rizzo et al. 2021](#); [Akins et al. 2025](#)).

The space telescope *JWST* is recently being used to probe the high redshift range in H $\alpha$  (and [OIII]) kinematics, with surveys such as JADES ([de Graaff et al. 2024a](#)), GA-NIFS ([Übler et al. 2024b](#); [Bertola et al. 2025](#); [Marconcini et al. 2024](#)) and others ([Barišić et al. 2025](#); [Danhaive et al. 2025b](#); [Fujimoto et al. 2025](#)).

### 1.2 Key Past results

Kinematic studies have been key in understanding how the dynamics of galaxies affect their evolution. A fundamental empirical scaling relation was found between the stellar (or baryonic) mass of a disk galaxy and its rotation velocity,  $M \propto V_{\text{rot}}^4$  (the “Tully-Fisher” relation) ([Tully & Fisher 1977](#); [McGaugh et al. 2000](#); [Lelli et al. 2016b, 2019](#); [Übler et al. 2017](#)), and has been shown to hold up to  $z \sim 3$ , with application both in calibrating cosmological simulations ([Vogelsberger et al. 2014](#); [Schaye et al. 2015](#); [Somerville & Davé 2015](#)) and as a cosmological distance measure ([Freedman et al. 2001](#); [Schombert et al. 2020](#); [Boubel et al. 2024](#)).

The velocity dispersion  $\sigma_0$  of the gas in the interstellar medium (ISM) increases with redshift, for both the ionized and molecular gas phases ([Übler et al. 2019](#); [Förster Schreiber & Wuyts 2020](#); [de Graaff et al. 2024b](#); [Lee et al. 2025a](#); [Danhaive et al. 2025b](#); [Wisnioski et al. 2025](#)). Consequently, at  $z \sim 2-3$  galaxies are typically less rotationally supported, as defined by the ratio of rotation velocity to their velocity dispersion,  $V/\sigma_0$ , which can become as low as  $\approx 2-4$  ([Förster Schreiber & Wuyts 2020](#)). Such conditions lead to gravitational fragmentation of the disk via “Toomre” instability, forming  $\sim$ kpc sized star forming clumps, which have been frequently observed ([Toomre 1964](#); [Burkert et al. 2010a](#); [Genzel et al. 2011](#); [Förster Schreiber et al., in prep.](#)). However, other studies, focused mostly on the cold gas phase, find velocity dispersions are much smaller and galaxies retain high rotation support of  $V/\sigma_0 \sim 10$  up to  $z \sim 4-5$  ([Rizzo et al. 2023, 2024](#); [Roman-Oliveira et al. 2024](#)). This tension is yet to be resolved; yet it is commonly agreed that the ionized gas is more turbulent than the molecular phase (e.g., [Girard et al. 2021](#)).

The characteristic flat outer disk rotation curves, observed in many local spiral galaxies, is one of the key evidences for the existence of dark matter in galaxies ([Rubin & Ford 1970](#); [Gunn 1980](#); [van Albada et al. 1985](#); [de Blok et al. 2008](#)). Dark matter amounts to most of the total mass for massive spirals in the local universe,  $\sim 40-80\%$  of the mass budget within the half-mass radius, and completely dominates the mass budget in dwarf galaxies ([Oh et al. 2011, 2015](#); [Lelli et al. 2016a](#)). Yet, this ubiquitous “flatness” indicates that the dark matter distribution has to be finely tuned to the baryonic content of the galaxy, a problem that became known as the “disk-halo conspiracy” (e.g. [van Albada & Sancisi 1986](#)).

The distribution of dark matter is commonly described using empirical and theoretical density profiles. The most widely adopted is the Navarro-Frenk-White (NFW) profile, a universal density profile arising from collisionless N-body simulations with an inner cusp scaling as  $\rho \propto r^{-1}$  ([Navarro et al. 1996](#); [Navarro et al. 1997, 2004](#)). However, other forms of dark matter profiles have been suggested, with varying inner power law slopes of the form  $\rho \propto r^{-\alpha}$ . These are typically split into cusps ( $\alpha \gtrsim 1$ ; such as the NFW profile) or cores ( $\alpha \approx 0$ ). A commonly used cored density profile is the “Burkert” pro-

file (Burkert 2015), suggest to fit local dwarf galaxies. Other profiles are parametrized in such a way to have either a cusp or a core, depending on the choice of parameters, such as the generalized-NFW (Zhao 1996), Einasto (Einasto 1965), or the Dekel-Zhao profile (Freundlich et al. 2020).

Including the effects of the baryons on the DM leads to complicating dynamics that can change the distribution of DM in the halo from the results of the idealized N-body simulations. On the one hand, the accumulation of baryons in the center of the halo causes the halo to further contract (“adiabatic contraction”), resulting in an inner DM cusp that is steeper than the NFW,  $\rho \propto r^{-\alpha}$  with  $\alpha > 1$  (e.g. Blumenthal et al. 1986). On the other hand, feedback processes and mergers inject energy that can lead to an expansion of the halo and form an inner core, i.e.  $\alpha \approx 0$ , a process most efficient in massive dwarf galaxies (Governato et al. 2012; Read et al. 2019; Lazar et al. 2020). Such DM cores have been observed in local dwarf galaxies (de Blok 2010; Oh et al. 2015), and some kinematic studies suggest they can also occur in massive galaxies at  $z \sim 1 - 2$  (Genzel et al. 2020; Bouché et al. 2022; Nestor Shachar et al. 2023).

### 1.3 Rotation curve modelling at high- $z$

At higher redshifts, both surface brightness dimming and limited angular resolutions have a significant impact on the kinematic maps. While the first can be overcome by long exposures (e.g. Genzel et al. 2017), the latter is harder to overcome as it is limited by instrumental capabilities and atmospheric turbulence. This leads to “beam smearing”, an artificial smoothing of velocity gradients and local kinematic features as light is convolved from large physical areas over the source. Beam smearing creates significant biases in the derived rotation curves if not properly accounted for in the modeling process, and has long been a challenge for analyzing rotation curves (e.g., Espejo Salcedo et al. 2025a).

To address these challenges, the community has developed sophisticated modelling tools that can be applied directly in observational space, thereby avoiding the systematic biases introduced by traditional 2D kinematic map extraction. Commonly used 3D tools are <sup>3D</sup>Barolo, GalPak<sup>3D</sup> and dysmalpy. Other tools, such as 2DBAT, employ a 2D modelling approach but are intended mainly for highly-resolved systems.

DysmalPy<sup>1</sup> (DYnamical Simulation and Modelling ALgorithm in PYthon), inspired by the earlier DISDYN program, is a forward modeling tool specifically designed for analyzing galaxy kinematics from modern IFU data cubes (Davies et al. 2004a,b; Cresci et al. 2009; Davies et al. 2011; Wuyts et al. 2016; Lang et al. 2017; Genzel et al. 2017; Übler et al. 2018; Price et al. 2021; Lee et al. 2025b). It uses analytical mass components to construct an axisymmetric model of a rotating galaxy, generating a full 4D hypercube containing a spectrum at each pixel. The galaxy is then rotated to match the sky projection, and is convolved over a finite beam to recover the line-of-sight spectra, fully incorporating all relevant observational and projection effects. It uses a Bayesian inference method (MCMC) to fit observational data.

GalPaK<sup>3D</sup>,<sup>2</sup> (Galaxy Parameters and Kinematics) is another parametric tool that is using Bayesian inference methods to fit observed data cubes (Bouché et al. 2015, 2021; Bacon et al. 2015; Mason et al. 2017; Szakacs et al. 2021; Ciocan et al. 2022; Puglisi et al. 2023; Birkin et al. 2024). However, instead of assuming the shape of

the mass distribution, it uses analytics shapes for the rotation (e.g.,  $v_{\text{rot}} \propto \tan^{-1}(r)$ ) and the emission profile (e.g., Sérsic profile), which are used to recover the kinematic and morphological properties. It was developed to work with 3D data cubes, recovering both geometric and kinematic properties.

<sup>3D</sup>Barolo<sup>3</sup> (3D-Based Analysis of Rotating Object via Line Observations) is a non-parametric tool developed to recover rotation velocities Di Teodoro & Fraternali (2015); Di Teodoro et al. (2016); Iorio et al. (2017); Rizzo et al. (2021, 2023); Deg et al. (2022); Westmeier et al. (2022); Roman-Oliveira et al. (2024). It uses tilted-ring models to recover the intrinsic rotation pattern directly from a data cube, while taking into account beam smearing and projection effects. It does not rely on assumptions about the mass distribution and allows flexibility in the shape of the inferred kinematic profiles.

While powerful, these 3D algorithms can become computationally expensive. It requires the construction of a full 3D cube (in the case of <sup>3D</sup>Barolo and GalPak<sup>3D</sup>) or a 4D hypercube (in dysmalpy), which is then collapsed and convolved over the sky orientation. This amounts to a total of  $n_x \times n_y \times n_z (n_{\lambda})$  points, at each implementation of the model. In a Bayesian inference framework, this has to be calculated repeatedly at each step. While this is useful to handle the degrees of freedom when simultaneously fitting multiple parameters, it can hamper the ability to test multiple forms of assumptions (i.e., priors, profile shapes, systematics, parameters co-dependency), in a time where galaxy samples are increasing in size.

Other kinematic tools enable 2D modeling, such as 2DBAT<sup>4</sup> Oh et al. (2018, 2020) and diskfit<sup>5</sup> Kuzio de Naray et al. (2012); Sellwood & Spekkens (2015), yet they are designed for highly-resolved systems in the Local Universe. They focus on accurate recovery of the geometrical properties of the galaxy, including the existence of warps, and detailed kinematic features arising from bars, spiral arms, or non-circular motions (Oh et al. 2022, 2025; Elagali et al. 2018; Kim et al. 2020; Zhang et al. 2020; Di Folco et al. 2020; Bewketu Belete et al. 2021; Wong et al. 2021; Bisaria et al. 2022; Oh & Wang 2025; Liu et al. 2025). Both tools are non-parametric, with 2DBAT using a tilted-ring approach and diskfit a global profile with no pre-assumed form. As these features require highly resolved observations, with high S/N, these tools have no beam smearing correction and are less relevant in the high- $z$  regime, where such corrections become critical.

In this paper, we present RotCurves<sup>6</sup>: a new modeling tool designed to fit galactic rotation curves using a parametric, forward modelling approach, allowing flexibility and fast computational time. This is accomplished by implementing a 2D approximation of the galactic midplane, which is convolved given the instrumental PSF and sky orientation. Instead of rotating the galaxy to align with the beam PSF (which would have to be done in 3D), we use the projection of the beam as it intersects the midplane of the galaxy for a given inclination angle. Our code is intended to recover the physical properties of a galaxy, with the effects of beam-smearing, but assuming its inclination and PA are already known. RotCurves is not intended to directly fit these geometric properties, but relies on having them estimated beforehand. We demonstrate the accuracy of our tool with synthetic datasets created with dysmalpy, discussing the effects on the various parameters.

The paper is structured as follows. In § 2 we describe the process

<sup>3</sup> <https://editeodoro.github.io/Bbarolo/>

<sup>4</sup> <https://github.com/seheonoh/2dbat>

<sup>5</sup> <https://kspekkens.github.io/DiskFit/>

<sup>6</sup> <https://github.com/nestoramit/RotCurves>

<sup>1</sup> <https://www.mpe.mpg.de/resources/ir/dysmalpy>

<sup>2</sup> <https://galpak3d.univ-lyon1.fr/>

of creating a mock rotation curve with **RotCurves**: the definition for the mass distribution and velocity profiles (2.1), pressure support corrections (2.2), the beam smearing process using our beam projection method (2.3), and the setup for the built-in MCMC fitting procedure (2.4). In § 3 we compare our results versus model generated with **dysmalpy**, comparing the beam smearing method for a fiducial model of a  $z = 2$  galaxy (3.1), the performance for various model parameters (3.2), the MCMC fitter (3.3), and the effects of simulated noise on the recovery of the physical parameters (3.4). In § 4 we summarize and discuss the results.

Throughout the paper we adopt a flat  $\Lambda$ CDM cosmology, with  $\Omega_m = 0.3$ ,  $\Omega_\Lambda = 0.7$  and  $H_0 = 70 \text{ km s}^{-1} \text{ Mpc}^{-1}$ .

## 2 MODEL OUTLINE

We construct an idealized model of a galaxy as an axisymmetric system in centrifugal equilibrium with all gaseous and stellar mass components in circular orbits. The rotation velocity is a function of the radius  $r$ , given by  $V_{\text{circ}}^2 = -r \frac{d\phi(r)}{dr}$ , where  $\phi$  is the gravitational potential. As the gravitational potential can be expressed as a linear combination of different mass distributions, this expression can be treated as a sum of the squared circular velocity of each of these components,  $V_{\text{circ}}^2 = \sum_i V_{i,\text{circ}}^2$ . We calculate the intrinsic velocity field within the midplane of the galaxy, so we only need two coordinates,  $(x_{\text{gal}}, y_{\text{gal}})$ , with the corresponding radius  $r_{\text{gal}} = \sqrt{x_{\text{gal}}^2 + y_{\text{gal}}^2}$  and angle with respect to the  $x$ -axis  $\theta_{\text{gal}} = \arctan(y_{\text{gal}}/x_{\text{gal}})$ . Given a composition of mass distributions, the circular velocity at each radius  $V_{\text{circ}}^2(r_{\text{gal}})$  is calculated analytically. We sample the grid uniformly in the  $xy$ -plane, with a squared pixel size with sides  $\Delta x_{\text{gal}} = \Delta y_{\text{gal}}$ . If only the intrinsic velocity field is of interest, the pixel resolution can be set arbitrarily but when fitting to observations it is best to match the model resolution to the instrumental pixel size.

### 2.1 Mass Distributions

We calculate the intrinsic circular velocity in the midplane of the galaxy in the presence of the various mass components included. Baryons are considered to be purely axisymmetric with no warping, split into two distinct components of a bulge and a disk, and the dark matter halo is considered to be spherically symmetric. In the following subsections we describe the formulation used for the different density profiles, and also their mass and velocity profiles. Each mass distribution has a characteristic scale-length  $r_s$  and total mass  $M$ . All functions are given by the normalized radius:

$$x \equiv r/r_s \quad (1)$$

In general, we describe the enclosed mass within radius  $x$  using a scale mass  $M_s$  and a dimensionless function  $f_M(x)$  such that:

$$M(< x) = M_s \times f_M(x) \quad (2)$$

The formula for the dimensionless function  $f_M(x)$  is discussed later, and differs for cylindrical and spherical cases.

The effective radius, or half mass radius, is the radius encompassing half the total mass of the profile, and is set by solving the implicit equation:

$$f_M(x_{\text{eff}}) = \frac{1}{2} f_M(x_{\text{max}}) \quad (3)$$

where  $x_{\text{max}}$  is the edge of the distribution, and is typically  $x_{\text{max}} \rightarrow \infty$ .

The circular velocity profile:

$$V_{\text{circ}}(x) = V_s \times f_V(x) \quad (4)$$

$$V_s = \sqrt{\frac{GM_s}{r_s}} \quad ,$$

with the characteristic velocity  $V_s$  dimensionless function  $f_V(x)$ , and  $G$  being the gravitational constant.

#### 2.1.1 Baryonic components

Axisymmetric mass distributions are best described by their local surface densities  $\Sigma(r)$ . We denote the central surface density as  $\Sigma_0$  and define a dimensionless density function in terms of the normalized radius defined in Equation 1:

$$\Sigma(x) = \Sigma_0 \times f_\Sigma(x) \quad (5)$$

where  $f_\Sigma(0) = 1$  and  $f_\Sigma(x_{\text{max}}) = 0$ . The scale mass  $M_s$  is given by

$$M_s = 2\pi\Sigma_0 r_s^2 \quad , \quad (6)$$

and the dimensionless mass function  $f_M(x)$

$$f_M(x) = \int_0^x t f_\Sigma(t) dt \quad , \quad (7)$$

with  $\Sigma_0$  normalized so that the total mass equals  $M$

$$\Sigma_0 = \frac{M}{2\pi r_s^2 f_M(x_{\text{max}})} \quad , \quad (8)$$

and  $x_{\text{max}} \rightarrow \infty$  by default.

The circular velocity for razor-thin mass distributions have to be calculated explicitly by the integrations (see [Binney & Tremaine 2008](#), Eq. 2.158-2.160):

$$f_V^2(x) = -x \int_0^\infty J_1(kr) k S(k) dk \quad (9)$$

$$S(k) = \int_0^\infty J_0(ku) f_\Sigma(u) u du \quad ,$$

where  $J_1$  and  $J_2$  are the Bessel functions.

If the distribution is razor-thin, Equations 5-8 are an exact description. However, in real galactic disks there is a finite thickness measured by the ratio,  $q_0$ , between the scale height and the scale length. In the Local Universe, disks of Milky Way like galaxies are close to razor-thin ( $q_0 \approx 0.05$ ) while at higher- $z$  disks tend to be more oblate ( $q_0 \approx 0.2$ ) ([Lian & Luo 2024](#); [Tsukui et al. 2025](#)). In the more general case, the surface density is

$$\Sigma(x) = 2 \int_0^\infty \rho(x, z) dz \quad (10)$$

where  $z$  is the vertical coordinate, and  $\rho(x, z)$  is the local volume density. The circular velocity can be calculate by decomposing the local density and integrating over iso-density surfaces. We Follow the method provided by [Noordermeer \(2008\)](#) to decompose Sérsic profiles, which are the most commonly type of profile for a disk or a bulge.

It is useful to define a radially dependent “virial” coefficient,  $\kappa(x)$ , to quantify the local velocity deviations from Keplerian motions, i.e., the circular velocities for the masses but enclosed within spheres:

$$\kappa(x) = \frac{f_V^2(x)}{f_M(x)/x} \quad . \quad (11)$$

In essence,  $\kappa(x)$  encodes the effect the geometry of the mass distribution has on the potential compared to the simple spherical case,

Profile	Parameters	$r_s$	intrinsic axis ratio	$f_\Sigma(x)$	$R_{\text{eff}}/r_s$	$M/M_s$
Exponential disk	$M, R_d$	$R_d$	0	$\exp\{-x\}$	1.68	1
Thick Sérsic disk	$M, R_d, n$	$R_d$	$q_0$	$\exp\{-x^{1/n}\}$	$b_n^n$	$\Gamma(2n)$
Gaussian Ring <sup>a</sup>	$M, R_p, \sigma_r$	$R_p$	0	$\exp\{-A(x-1)^2\}$	$\approx 1 + \frac{1}{4}h^{-5/4}$	$\frac{1}{2A} \left( e^{-A} + \sqrt{\pi A} + \sqrt{A} \gamma\left(\frac{1}{2}, A\right) \right)$ $\approx (h - 0.07)^{-1}$

**Table 1.** Dimensionless properties of the surface density profiles included, as a function of the normalized radius  $x = r/r_s$ . <sup>a</sup>For the gaussian Ring profile we define:  $A = R_p^2/2\sigma_r^2$  and  $h = \sqrt{A}/2\sqrt{\ln 2}$ .

Profile	$f_M(x)$	$f_V^2(x)$
Exponential disk	$1 - e^{-x} (1 + x)$	$\frac{1}{2}x^2 \left[ I_0\left(\frac{x}{2}\right) K_0\left(\frac{x}{2}\right) - I_1\left(\frac{x}{2}\right) K_1\left(\frac{x}{2}\right) \right]$
Thick Sérsic disk	$\gamma(2n, x^{1/n})$	$\frac{2b_n^{n+1}}{\pi n^2} \times \int_0^x \frac{m^2}{\sqrt{x^2 - m^2(1 - q_0^2)^2}} \left[ \int_m^\infty \frac{e^{-bn_1^{1/n} t^{1/n-1}}}{t^{2-m^2}} dt \right] dm$
Gaussian Ring <sup>a</sup>	$\frac{1}{2A} \left[ e^{-A} - e^{-A(x-1)^2} \right] + \frac{1}{2\sqrt{A}} \left[ \gamma\left(\frac{1}{2}, A\right) + \gamma\left(\frac{1}{2}, A(x-1)^2\right) \text{sgn}(x-1) \right]$	$2A \times \int_0^x \frac{m}{\sqrt{x^2 - m^2}} \left[ \int_0^\infty e^{-A(x-1)^2} \frac{m(t-1)}{\sqrt{t^2 - m^2}} dt \right] dm$

**Table 2.** Table 1 cont.

for which  $\kappa(r) = 1$  (see also [Price et al. 2022](#), for a similar definition). At large radii, we expect this parameter to approach unity  $\kappa(x \rightarrow \infty) = 1$ .

The light distribution of the baryon component follows the surface density with a constant mass-to-light ratio

$$I(r) = \Upsilon \times \Sigma(r) , \quad (12)$$

in arbitrary units, as only the relative flux is important for the process of the beam smearing. By default we set  $\Upsilon = 1$  for baryonic components. If no light is emitted with respect to the tracer,  $\Upsilon = 0$ . For example, if considering a combination of disk and bulge in H $\alpha$  emission, it is reasonable to assume the disk overshadows the bulge  $\Upsilon_{\text{disk}} \gg \Upsilon_{\text{bulge}}$ . It is also possible to construct various combinations in which the M/L does not trace the mass completely, such as an emission ring above a faint exponential disk (see [Nestor Shachar et al. 2025](#)).

While the physical distribution of various tracers might differ from that of the stellar disk, these difference are mitigated by the beam smearing in low-resolution studies. At high-z the common tracers are the ionized and molecular phases of the ISM, which although linked to sites of star-formation are typically widespread enough throughout the disk so that, when smeared, can become quite smooth (e.g., [Übler et al. 2018](#); [Jones et al. 2025](#)). The assumption of a constant M/L has been used successfully in multiple kinematic studies ([Genzel et al. 2017, 2020](#); [Price et al. 2021](#); [Nestor Shachar et al. 2023](#); [Herrera-Camus et al. 2022](#); [Lee et al. 2025a](#)).

### 2.1.2 Dark Matter Halos

We assume spherically symmetric dark matter halos uniquely defined by redshift  $z$ , virial mass  $M_{\text{vir}}$  and concentration parameter  $c$  (along with possible additional parameters in the density profile). For a local density  $\rho_{\text{DM}}(r)$  and scale length ( $r_s$ ), we define similarly to Equation 5 the dimensionless density function

$$\rho(x) = \rho_0 \times f_\rho(x) , \quad (13)$$

the scale mass

$$M_s = \frac{4\pi}{3} \rho_0 r_s^3 , \quad (14)$$

and the formula for the dimensionless enclosed mass within radius  $x$

$$f_M(x) = 3 \int_0^x t^2 f_\rho(t) dt . \quad (15)$$

Any halo extends to the virial radius  $R_{\text{vir}}$ , the radius within which the average matter density is  $\Delta$  times the critical density of the Universe at redshift  $z$ ,  $\rho_{\text{crit}} = \frac{3H^2(z)}{8\pi G}$ . The enclosed mass within  $R_{\text{vir}}$  is then the virial mass of the halo, and is by definition:

$$M_{\text{vir}} = \frac{4\pi}{3} \Delta \rho_{\text{crit}}(z) R_{\text{vir}}^3 . \quad (16)$$

Typical values for the virial overdensity are  $\Delta = (100, 177, 200)$ , and we use  $\Delta = 200$  as the default value (see for example [Bullock et al. 2001](#)). The concentration parameter

$$c = R_{\text{vir}}/r_s \quad (17)$$

is the ratio of the virial radius to the scale radius for the dark-matter density distribution, and this ratio quantifies the “compactness” of the halo. Using Equations 2, 15 and 16 we can write the central density in terms of  $z$ ,  $M_{\text{vir}}$ ,  $c$  as

$$\rho_0 = \frac{c^3}{f_M(c)} \Delta \rho_{\text{crit}}(z) . \quad (18)$$

For a spherical mass distribution, regardless of the specific profile, the circular velocity at radius  $r$  is the Keplerian  $V_{\text{circ}}^2 = GM(< r)/r$ , and the dimensionless velocity function is:

$$f_V(x) = \frac{f_M(x)}{x} . \quad (19)$$

As baryons accumulate in the center of the halo (i.e., a galaxy forms), additional force acting on the inner halo would lead it to contract. Assuming galaxy assembly is slow and continuous, the contraction can be treated as adiabatic. Following [Mo et al. 1998](#), the final (contracted) halo profile can be solved by requiring conservation of angular momentum for each DM particle, assuming pure circular orbits and no shell crossings:

$$x M_f(< x) = x_i M_i(< x_i) \quad (20)$$

where  $x_i$  is the initial radius and  $x$  the radius after contraction, in a

Profile	Parameters	$r_s$	$f_\rho(x)$	$f_M(x)$
NFW	$M, R_{\text{vir}}, c$	$R_{\text{vir}}/c$	$\frac{1}{x(1+x)^2}$	$\frac{3}{1+x} \left[ \ln(1+x) - \frac{x}{1+x} \right]$
$\alpha$ -NFW	$M, R_{\text{vir}}, c, \alpha$	$R_{\text{vir}}/c$	$\frac{1}{x^\alpha(1+x)^{3-\alpha}}$	$\frac{3}{3-\alpha} \left[ x^{3-\alpha} {}_2F_1(3-\alpha, 3-\alpha; 4-\alpha; -x) \right]$
Burkert	$M, R_{\text{vir}}, c$	$R_{\text{vir}}/c$	$\frac{1}{(1+x)(1+x^2)}$	$\frac{3}{2} \left[ \frac{1}{2} \ln(1+x^2) + \ln(1+x) - \arctan(x) \right]$
Einasto	$M, R_{\text{vir}}, c, n$	$R_{\text{vir}}/c$	$\exp\{-x^{1/n}\}$	$3n \gamma(3n, x^{1/n})$
Dekel-Zhao	$M, R_{\text{vir}}, c$	$R_{\text{vir}}/c$	$\frac{3-a}{3} \left( 1 + \frac{3-\bar{g}}{3-a} x^{1/b} \right) \frac{1}{x^a (1+x^{1/b})^{1+b(\bar{g}-a)}}$	$\frac{x^3}{x^a (1+x^{1/b})^{b(\bar{g}-a)}}$

**Table 3.** Density profile for the dark matter. We assume spherically symmetric distributions, described with the normalized radius  $x = r/r_s$  (see Equation 1). The dimensionless circular velocity for all profiles is  $f_V(x) = \sqrt{f_x(x)}/x$  (see Equation 4).

system including the baryons. The total DM mass remains the same within  $x$  as is within the initial  $x_i$ , so that equation 20 becomes:

$$x (M_{\text{baryons}}(< x) + M_i(< x_i)) = x_i M_i(< x_i). \quad (21)$$

We can solve for the “contraction factor”  $\eta(x) \equiv x/x_i$ , for which the last equation can be rearranged as:

$$\eta^{-1}(x) = 1 + \frac{M_{\text{baryons}}(< x)}{M_i(< x/\eta(x))}. \quad (22)$$

The last equation can be solved numerically given the distribution of baryons. This contraction factor must be smaller than unity at all radii and approach it as  $r \rightarrow R_{\text{vir}}$ , as the outer halo is expected to be less affected by the centrally concentrated baryons. Using the contraction factor, the final density distribution is found by plugging the initial radius  $x/\eta$ :

$$\rho_{\text{cont}}(x) = \rho_i(x/\eta(x)) \quad (23)$$

with  $\rho_i$  the initial halo profile before contraction, i.e., as given by equation 13.

### 2.1.3 Light distributions

The flux distribution

## 2.2 Pressure Support

Pressure gradients introduce additional forces that act on the individual mass elements, which can become dynamically significant (Burkert et al. 2010b). Typically, the ISM gas has velocity dispersions ranging from  $\sim 20$  km/s at  $z = 0$ , to  $\sim 60$  km/s at redshifts  $z \approx 3$ , and can become dynamically important as it introduces a pressure term that changes the equilibrium velocity.

The hydrostatic equilibrium equation for gas in a turbulent disk is (Burkert et al. 2010a):

$$\frac{V_{\text{rot}}^2(r)}{r} = F_g(r) + \frac{1}{\rho(r)} \frac{dP(r)}{dr} \quad (24)$$

where  $V_{\text{rot}}(r)$  is the equilibrium circular velocity,  $F_g(r)$  is the gravitational force at  $r$ , and  $\rho(r)$  is the gas density. The pressure  $P = \rho(\sigma^2 + c_s^2)$  has a kinetic component originating from the isotropic velocity dispersion  $\sigma$  and a thermal component dependent on the sound speed  $c_s$ , which can be neglected as typically  $c_s \ll \sigma$ . If we denote  $V_{\text{circ}}$  as the circular velocity due to gravity alone (i.e., for  $P = 0$ ), the pressure-corrected (observable) rotational velocity  $V_{\text{rot}}$  can be written as:

$$V_{\text{rot}}^2(x) = V_{\text{circ}}^2(x) + \sigma^2 \frac{d \ln(f_\rho \sigma_0^2)}{d \ln x} \quad (25)$$

where we have used Eq. (13) and switched to the normalized radius

$x = r/r_s$ . The importance of the pressure term is typically quantified using the velocity-to-dispersion ratio,  $V/\sigma_0$ . For high values the pressure gradients are negligible and the rotation is purely gravitationally supported (a “cold disk”). For ratios below  $\lesssim 2-3$  the disk is marginally stable and pressure gradient are important (a “hot disk”, Förster Schreiber & Wuyts 2020). Furthermore, at low  $V/\sigma$  the disk can become gravitationally unstable and form clumps at the Toomre scale (Toomre 1964). While these clumps produce asymmetries in the overall mass distribution, the clump’s masses ( $10^8 - 10^9 M_\odot$ ) are generally too small to strongly affect the global gravitational potential. Other effects, such as inward migration due to torques exerted on the clumps, can create deviations from circular motions (Romeo et al. 2010; Dekel et al. 2022). Such inflows have been observed in several clumpy  $z \sim 1-2$  galaxies, with velocities of 50–100 km/s ( $\approx 10-30\%$  of the circular velocity) (Genzel et al. 2023; Pastras et al. 2025; Jolly et al., in prep.). We ignore any such inflow motions in the modelling, as these higher-order kinematic corrections are smaller along the kinematic major-axis.

Two additional approximations are typically applied to Equation 25. One possibility is to assume that the velocity dispersion is independent of radius,  $\sigma = \text{const.} \equiv \sigma_0$ , giving (Burkert et al. 2010b):

$$V_{\text{rot}}^2(x) = V_{\text{circ}}^2(x) + \sigma_0^2 \frac{d \ln f_\rho(x)}{d \ln x} \quad (26)$$

A second possibility is to assume vertical hydrostatic equilibrium (HSE), for which the local midplane density is proportional to the total surface density  $\Sigma$  and the vertical velocity dispersion  $\sigma_z$ , namely,  $\rho = \frac{\pi G \Sigma^2}{2 \sigma_z^2}$  (a “Spitzer disk”, Spitzer 1942; Binney & Tremaine 2008). In the case of an isotropic velocity dispersion, the radial and vertical velocity dispersion are equal  $\sigma_z = \sigma_r \equiv \sigma$ , giving

$$V_{\text{rot}}^2(x) = V_{\text{circ}}^2(x) + 2\sigma^2 \frac{d \ln f_\Sigma(x)}{d \ln x}, \quad (27)$$

where  $f_\Sigma(x)$  is the surface density at radius  $x$ . Interestingly, equation 27 is also valid for radially changing velocity dispersions, as long as it can be locally treated as isotropic. Assuming HSE is a convenient assumption when dealing with observations, as it allows to directly use a surface density profile (e.g., an exponential disk) without knowing the intrinsic local 3D density. For a Sérsic disk,  $\ln f_\Sigma = -(r/R_d)^{1/n}$ , and Eq. (27) gives (Burkert et al. 2016):

$$V_{\text{rot}}^2(r) = V_{\text{circ}}^2(r) - 2b_n \sigma_0^2 (r/R_{\text{eff}})^{1/n} \quad (28)$$

where  $R_{\text{eff}}$  is the disk half mass radius, and  $b_n \approx 2n - \frac{1}{3}$  is the solution to  $\gamma(b_n, 2n) = \frac{1}{2}\Gamma(2n)$  with  $\gamma$  and  $\Gamma$  being the incomplete and complete gamma function, respectively (Ciotti & Bertin 1999).

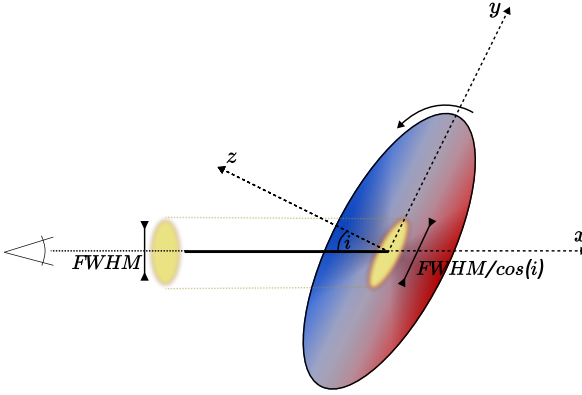


**Figure 1.** Illustration of the 2D beam smearing projection for an inclination angle  $i$ . As the galaxy becomes more edge-on ( $i \rightarrow 90^\circ$ ), it intersects larger areas on the disk plane. The projected ellipse has an axis-ratio of  $a/b = 1/\cos i$  (for  $i \neq 90^\circ$ ).

### 2.3 Sky projection

After generating an intrinsic velocity profile in the galactic plane, we want to simulate the observed velocity map for a given sky orientation and finite beam resolution. This is typically done by rotating the coordinates in the frame of the galaxy to sky coordinates, given the inclination angle, then summing over the line-of-sight to create the two dimensional velocity map. This is followed by convolution with an instrumental point spread function (PSF). Treatment of this beam smearing effect is crucial, as large PSF sizes can cause dramatic effects on the resulting velocity map, and often can be very time consuming since the number of pixel scales rapidly as  $\propto n^3$ . Hence, instead of rotating the galaxy coordinates to match the sky coordinates, in `RotCurves` we replace the PSF with an “effective beam”, as a function of the inclination angle while still working in galactic coordinates. We illustrate this in Figure 1. For example, a circular PSF through a face-on galaxy imprints a circle. For a more edge-on galaxy the beam intersects the galactic plane at an angle and it imprints a prolate ellipse. If the galaxy is axisymmetric, we can arbitrarily set the  $x_{\text{gal}}$  axis as the rotation axis for the inclination, so that the change is only applied to the  $y_{\text{gal}}$  axis. Specifically, if we consider a circular Gaussian PSF with a standard deviation  $\sigma_{\text{PSF}}$ , it will become a bi-variate Gaussian with  $(\sigma_x, \sigma_y) = (\sigma_{\text{PSF}}, \sigma_{\text{PSF}}/\cos(i))$ . This way a face-on projection ( $i = 0$ ) results in a circular shape, while the edge-on case ( $i = 90$ ) results in a cylinder.

The observed rotation velocity is then calculated as a weighted average over the area of the “effective beam”. In addition to the PSF, the strength of the emission itself has to be taken into account. As kinematic observations typically use emission line tracers, it will not be isotropic and will tend to favor certain areas in the galaxy. For example, 21cm hydrogen emission arises from the neutral ISM covering most of the stellar disk, while H $\alpha$  emission is emitted from hot  $\sim 10^4$ K clouds around young OB stars, tracing recent star formation. Therefore, “light weighting” is included in this step, with a functional form for the emission,  $I(r)$ . By default, we assume a constant mass-to-light (M/L) ratio following the density profile of the disk. In addition, only line-of-sight velocities contribute observationally, introducing an additional  $\cos \theta$  factor.

In total, the observed velocity at a given radius  $r$  is just the weighted

average:

$$V_{\text{obs}} \equiv \langle V_{\text{circ}}(r) \rangle = \frac{\sum_{x,y} \text{PSF}(x_{\text{gal}}, y_{\text{gal}}) I(r_{\text{gal}}) V_{\text{circ}}(r_{\text{gal}}) \cos \theta}{\sum_{x,y} \text{PSF}(x_{\text{gal}}, y_{\text{gal}}) I(r_{\text{gal}})} \quad (29)$$

and the velocity dispersion at a given radius  $r$  is estimated as the weighted standard deviation over the “effective” PSF:

$$\sigma_{\text{obs}} = \sqrt{\langle V_{\text{circ}}^2 \rangle - V_{\text{obs}}^2} \quad (30)$$

summing over all  $(x_{\text{gal}}, y_{\text{gal}})$  within the FWHM of the PSF, where  $r_{\text{gal}} = \sqrt{x_{\text{gal}}^2 + y_{\text{gal}}^2}$  and  $\cos \theta = \arctan(y_{\text{gal}}/x_{\text{gal}})$ .

### 2.4 MCMC Fitting

The sky-projected velocity map can be fitted to an observed velocity map using a Monte-Carlo Markov-Chain (MCMC) Bayesian algorithm implemented with the python package `emcee` (Foreman-Mackey et al. 2013a) together with `corner` to analyze the posterior distribution (Foreman-Mackey 2016). We can then simultaneously fit multiple free parameters and estimate their distribution given constraints on both observational data and priors (via scaling relations, other observational constraints, etc.). It does so by generating a Markov chain in which each new proposed state is accepted or rejected based on a probabilistic criterion, maximizing the log-probability function. Using many iterations, the walkers explore the posterior distribution of the free parameters and provide realistic estimates of the uncertainties, given the walkers are not correlated and the chain has converged. The best fit values are estimated as the median or the maximum of the posteriors, and even though these might not optimally maximize the log-likelihood they provide good estimates.

For a set of  $n$  free parameters, the MCMC algorithm constructs a sequence of parameter states  $\vec{\theta} = (\theta_1, \theta_2, \dots, \theta_n)$ , each sampled from an initial (prior) distribution  $\mathcal{P}(\theta_i)$ . Given  $\vec{\theta}$ , a galaxy model is constructed along with its projected, mock-observed rotation curve, as discussed in the previous paragraphs. At each step, the MCMC algorithm is attempting to minimize the log-probability function, which is the sum of the log-prior of each free parameter and the log-likelihood as defined by a least-squares:

$$\ln \mathcal{L} = -\frac{1}{2} \sum_{i=1}^m \left( \frac{v_{\text{data},i} - v_{\text{rot},i}(\vec{\theta})}{v_{\text{err},i}} \right)^2 \quad (31)$$

$$+ \sum_{j=1}^n \mathcal{P}(\theta_j) \quad (32)$$

with  $m$  data points, and where  $\vec{\theta}$  are the  $n$  model parameters.

The priors are set for each parameter independently, and are drawn either from a uniform or a Gaussian probability distributions, both bounded by minimum and maximum values:

$$\ln \mathcal{P}(\theta) = \begin{cases} -\infty, & \theta < \theta_{\min}, \theta > \theta_{\max} \\ 0, & \text{uniform} \\ -\frac{1}{2} \left( \frac{\theta - \theta_0}{\sigma_\theta} \right)^2, & \text{Gaussian} \end{cases} \quad (33)$$

with  $\theta_0$  the Gaussian center (by default the initial value) and  $\sigma_\theta$  the standard deviation.

Each walker then makes a random step, repeating the process and attempting to maximize the log-likelihood while still allowing for occasional “bad” steps that would help if the walker is stuck at local

minima. We find that a combination of different steps is best to ensure rapid exploration of the parameter space and break correlated steps: each step has a 60% chance of being a `emcee.moves.StretchMove` with  $a_{\text{stretch}} = 2$ , 30% chance of being a `emcee.moves.DEMove` and 10% chance for a `emcee.moves.KDEMove`.

To properly sample the posterior space, a large number of individual “walkers” are required with a total number of iterations (or steps). We estimate the auto-correlation time  $\tau$  of the walkers for each parameter using the built-in method `sampler.get_autocorr_time`, and choose the maximum value as our estimate. The total number of steps is chosen to be much larger to ensure independent sampling,  $n_{\text{steps}} \approx 50\tau$ , of which the first  $n_{\text{burn}} \approx 5\tau$  are discarded as burn-in steps. With this number of steps, we set the number of walkers to be  $n_{\text{walkers}} = 100$  ensuring we have over  $\sim 3000$  independent samples ( $> 1000$ ) in the posterior distribution.

The best-fit values for each parameter are estimated as the median of the distribution, and the lower (upper) uncertainty is defined as the 16<sup>th</sup> (84<sup>th</sup>) percentiles of the posterior. If the posterior distribution is highly asymmetric, which can often be the case, the median might be significantly different than the value of maximum probability, and the maximum a-posteriori (MAP) might be a better estimator for the best-fit value.

### 3 BENCHMARK

We use the widely-used, publicly available, parametric code `Dysmalpy` to compare the results of our beam smearing process. `Dysmalpy` has been used in the literature to analyze rotation curves at high redshift multiple times with great success (Genzel et al. 2006; Wuyts et al. 2016; Lang et al. 2017; Genzel et al. 2017; Übler et al. 2018, 2024b,a; Price et al. 2021; Liu et al. 2023b; Posses et al. 2024; Telikova et al. 2025; Fei et al. 2025, Espejo Salcedo et al., in prep.). The code is described in detail in Price et al. (2021) and Lee et al. (2025b). Essentially, `dysmalpy` constructs a model of an idealized, axisymmetric rotating galaxy, comprised of multiple mass components, each with a defined functional form (e.g., a Sérsic profile) and a set of parameters (such as mass, effective radius, etc.). Given a combination of mass components, a full 3D cube of the galaxy is constructed, where each pixel contains a Gaussian distribution of velocities centered around the rotational velocity,  $V_{\text{rot}}$ , with a standard deviation of the intrinsic velocity dispersion of the gas,  $\sigma_0$ . The beam smearing is done for this 4D-hypercube, i.e.  $(x_{\text{gal}}, y_{\text{gal}}, z_{\text{gal}}, v)$ , by rotating it to sky coordinates and calculating the line-of-sight emission profile, taking into account the line-spread-function (LSF), point-spread-function (PSF) and the flux-weighting (or M/L ratio).

Using `dysmalpy` allows us to isolate the effect of the beam smearing correction alone, as we can define an intrinsically identical model for the galaxy and use similar pixel scales and box sizes to directly compare the recovered physical parameter of the galaxy. In contrast, other kinematic modelling tools (mentioned in § 1.3) do not assume an underlying mass profile but use either non-parametric tilted-ring approaches or purely mathematical forms (e.g.,  $v_{\text{rot}} \propto \tan^{-1}(r)$ ). This is important for our setup, as such these underlying differences can lead to systematics beyond the scope of this comparison (e.g., Lee et al. 2025b; Yttergren et al. 2025). The implementation of the beam smearing correction has been the subject of some debate in recent years, and the “correct” answer is very elusive as the “true” kinematic values of a galaxy remain unknown. Lee et al. (2025b) used a sample of observationally-motivated mock-observed galaxies to demonstrate that all three codes are in excellent agreement for the recovered velocity profile in the high signal-to-noise regime, with

Code	$n_{\text{pix}}$	pixel size [mas]	runtime [ms]
RotCurves	95	50	20
<code>dysmalpy</code>	95	50	3638

**Table 4.** Average runtimes of the beam-smearing correction for the fiducial model, calculated from  $n = 100$  procedures ( $\lesssim 1\%$  statistical error) on a single CPU. `RotCurves` generates a  $(n_{\text{pix}}, n_{\text{pix}})$  grid whereas `dysmalpy` generates a  $(n_{\text{pix}}, n_{\text{pix}}, n_{\text{pix}}, n_{\text{spec}})$  hyper-cube, with  $n_{\text{spec}} = 200$ . The beam FWHM is 10 pixels.

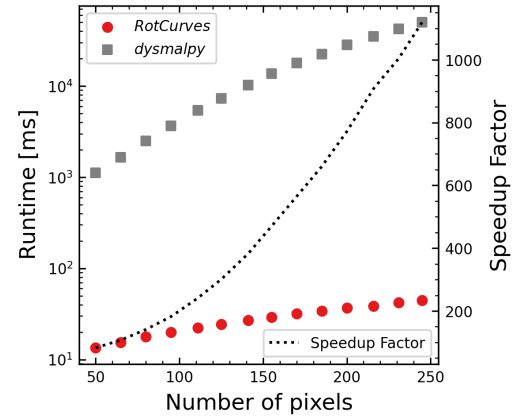


**Figure 2.** Average runtime of `RotCurves` (red circles) and `dysmalpy` (grey squares) as a function of the number of pixels on one side of the grid. Runtimes are calculated as the average CPU time from 100 computations. The speedup factor is shown in a dashed line, corresponding to the right side of the figure. `RotCurves` keeps under  $\lesssim 100\text{ms}$  even when resolving finely sampled grids, and is  $\approx 300 - 2500$  faster than `dysmalpy`.

less than a  $< 10\%$  difference in the recovered properties up to twice the effective radius.

We mention that 2DBAT in particular, with its 2D approach and similar Bayesian inference framework, make a good candidate for comparison. However, 2DBAT does not include the crucial beam smearing correction needed for interpreting high- $z$  observations. 2DBAT also assumes that the halo dominates the gravitational potential at all radii, making it more suitable for highly dark-matter dominated systems (Oh et al. 2018). At Cosmic Noon, there are many galaxies with very low contributions of dark matter on galactic scales, and `RotCurves` is built to support a wide variety in velocity profiles (Genzel et al. 2017, 2020; Nestor Shachar et al. 2023; Lee et al. 2025a; Danhaive et al. 2025a). Furthermore, the strength of 2DBAT is in the recovery of detailed non-axisymmetric features through varying PA and inclination with the tilted-ring approach, which differ fundamentally from the assumptions made in `RotCurves`, in which the galaxy is axisymmetric and the PA and inclination do not vary radially. In this paper we focus on how `RotCurves` recover the physical parameters of the galaxy, and not its geometric properties, making such comparisons beyond the scope of this current work.

Therefore, we limit our comparison to `dysmalpy` alone, as a more apples-to-apples approach for testing and comparing our parametric forward modelling code.

### 3.1 Beam smearing

The procedure for beam smearing is much more detailed in `dysmalpy` with its full 4D-hypercube, so we expect any differences in the mock-

Component	Parameter	Fiducial Value
Cosmology	Redshift	2
Disk	kpc-to-arcsec	8.4
	Mass [ $M_\odot$ ]	$3 \times 10^{10}$
	$R_{\text{eff}}$ [kpc]	4
	$n_s$	1
	$q_0$	0.2
Bulge	$\Upsilon$	1
	Mass [ $M_\odot$ ]	$10^{10}$
	$R_{\text{eff}}$ [kpc]	1
	$n_s$	4
	$q_0$	1
NFW Halo	$\Upsilon$	$10^{-2}$
	$f_{\text{DM}}(R_{\text{eff}})$	0.28
	Mass [ $M_\odot$ ]	11.8
	concentration	4.5
Pressure Support	$V_{\text{circ}}(R_{\text{eff}})/\sigma_0$	4
	$\sigma_0$ [km/s]	56
Geometry	inclination	60
Beam	FWHM/ $R_{\text{eff}}$	0.5
	FWHM ["]	0.25
	pixel size [mas]	50

**Table 5.** Parameters for the fiducial model including an exponential disk, a de-Vaucouleurs bulge and an NFW halo, motivated by observational properties of massive SFGs at  $z \sim 2$  (Genzel et al. 2020; Nestor Shachar et al. 2023; Übler et al. 2019) and by cosmological scaling relations (Dutton & Macciò 2014; Moster et al. 2018). The mass includes both stellar and gas contents, assumed to have a similar distribution.

observed rotation curves to increase as the inclination becomes more edge-on (high  $i$ ), or as the PSF FWHM increases.

For comparisons, we construct a fiducial model consisting of an NFW dark matter halo, an exponential disk, and a bulge, with values typical for massive, star-forming galaxies at  $z = 2$ , and with a constant velocity dispersion for the gas (see Table 3.1). Motivated by large  $\text{H}\alpha$  IFU surveys of massive SFGs (e.g. Förster Schreiber et al. 2009; Wisnioski et al. 2015) we set the mass of the disk to  $M_{\text{disk}} = 5 \times 10^{10} M_\odot$ , comprising both stellar and gas content, with an effective radius of  $R_{\text{eff}} = 5$  kpc. We assume an intrinsic axis-ratio of  $q_0 = 0.2$  to account for disk thickness (Hamilton-Campos et al. 2023). We set the central bulge mass to  $M_{\text{bulge}} = 3 \times 10^{10} M_\odot$  (bulge-to-total ratio of 0.38), with a de-Vaucouleurs profile ( $n_s = 4$ ) and an effective radius of  $R_{\text{eff}} = 1$  kpc. We assume an NFW density profile for the dark matter halo, with concentration parameter  $c = 4.5$  appropriate for redshift  $z = 2$  (e.g. Dutton & Macciò 2014; Genzel et al. 2020; Nestor Shachar et al. 2023; Puglisi et al. 2023). For this halo the dark-matter fraction at  $R_{\text{eff}}$  is  $f_{\text{DM}} = 0.28$ .

Table 3 shows the average runtimes of each code as a function of the number of pixels and the size of the beam. RotCurves generates a mock-observed rotation curve at a scale of  $\sim 10\text{ms}$ , while dysmalpy will generate the same rotation curve at a scale of  $\sim 10\text{s}$ , the exact numbers depending on the number of pixels. Figure 2 shows that the runtime for RotCurves increases slowly with the number of pixels and is  $\lesssim 100\text{ms}$  even for a large number of pixels. On reasonable pixels scales and FOV sizes, RotCurves performs  $\approx 200 - 300$  times faster than dysmalpy, improving further as the grid increases in size. This boost in performance allows running high-resolution and large-scale models much faster, increasing the ability to test multiple scenarios. Runtime increases with increasing number of pixels, yet it increases slower for RotCurves than dysmalpy.

Comparing the two beam-smeared rotation curves in Figure 3, we find very good agreement between RotCurves and dysmalpy. Up to 3 times the effective radius, the difference does not exceed 5%, in

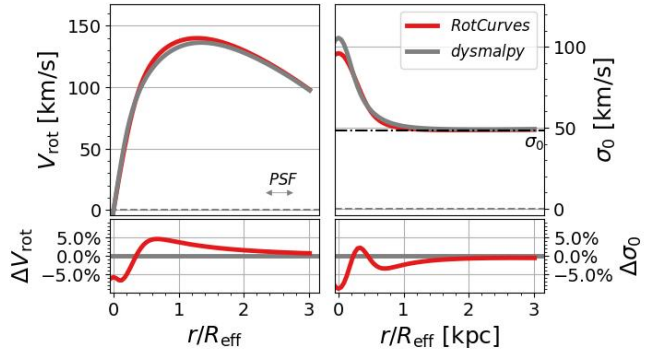


**Figure 3.** Mock-observed rotation (left) and dispersion (right) curves for RotCurves (red) and dysmalpy (black). The bottom panels show the residuals relative to dysmalpy. A PSF FWHM of  $0.25''$  ( $0.5R_{\text{eff}}$ ) is considered, comparable to ground-based high- $z$  spectroscopy. The residuals are  $\lesssim 5\%$  for both rotation and dispersion, with largest deviations at  $\approx 0.5R_{\text{eff}}$ . The root mean square error (in km/s) for the full curves is given in the top-left corner.

both rotation velocity and velocity dispersion. Beyond the effective radius, at  $r \approx 1 - 3R_{\text{eff}}$ , the RC is highly accurate with deviations as small as  $\lesssim 3\%$ . The inner part is more susceptible to differences, as the intrinsic large velocity gradients make the vertical scale more important. Yet even at  $r < R_{\text{eff}}$  deviations do not exceed 5%. In dysmalpy the beam collects light from particles off the midplane, and due to the inclination angle they will have larger radial distances that alter the line velocity centroids and broaden the line. Further out, and especially after the turnover radius, the off-midplane contribution will have both higher and lower velocities (i.e., closer and further radii). For a dropping rotation curve this leads to a lower centroid velocities, and vice versa for a rising curve.

Such effects are not included in RotCurves as it considers only midplane motions, and the velocities may be over-estimated, and dispersions under-estimated, compared to dysmalpy. However, as shown for our fiducial model, these differences are only at the  $\sim$ few percent level. A major contribution to the differences, mainly at large radii, is that dysmalpy assumes an exponentially dropping light profile in the  $z$ -direction, with the scale height tied to the effective radius of the disk,  $h_z \sim q_0 R_d \sim 0.1 R_{\text{eff}}$ . Therefore, this correction becomes important only when velocity gradients are large enough over  $\sim 3h_z$ , which is typically the case around the area of the bulge, but it is not the case further out in the disk. For the fiducial model,  $h_z \sim 400\text{ pc} = 0.1 R_{\text{eff}}$ .

### 3.2 Parameter study

To examine RotCurves over a wide range of model parameters, we examine how relative residuals react when varying a single parameter while keeping the rest fixed (as described in Table 3.1). The residuals are

$$\Delta V_{\text{rot}}(r_{\text{ap}}) = \frac{V_{\text{rot}}^{\text{Rotcurve}}(r_{\text{ap}}) - V_{\text{rot}}^{\text{dysmalpy}}(r_{\text{ap}})}{V_{\text{rot}}^{\text{dysmalpy}}(r_{\text{ap}})}$$

$$\Delta \sigma(r_{\text{ap}}) = \frac{\sigma^{\text{Rotcurve}}(r_{\text{ap}}) - \sigma^{\text{dysmalpy}}(r_{\text{ap}})}{\sigma^{\text{dysmalpy}}(r_{\text{ap}})} .$$

Figure 4 shows the velocity and velocity dispersion residuals at three locations representing the inner and outer parts of the galaxy,  $(0.5, 1, 2) \times R_{\text{eff}}$ , as a function of one parameter of the model. We focused on parameters that either have a physical importance

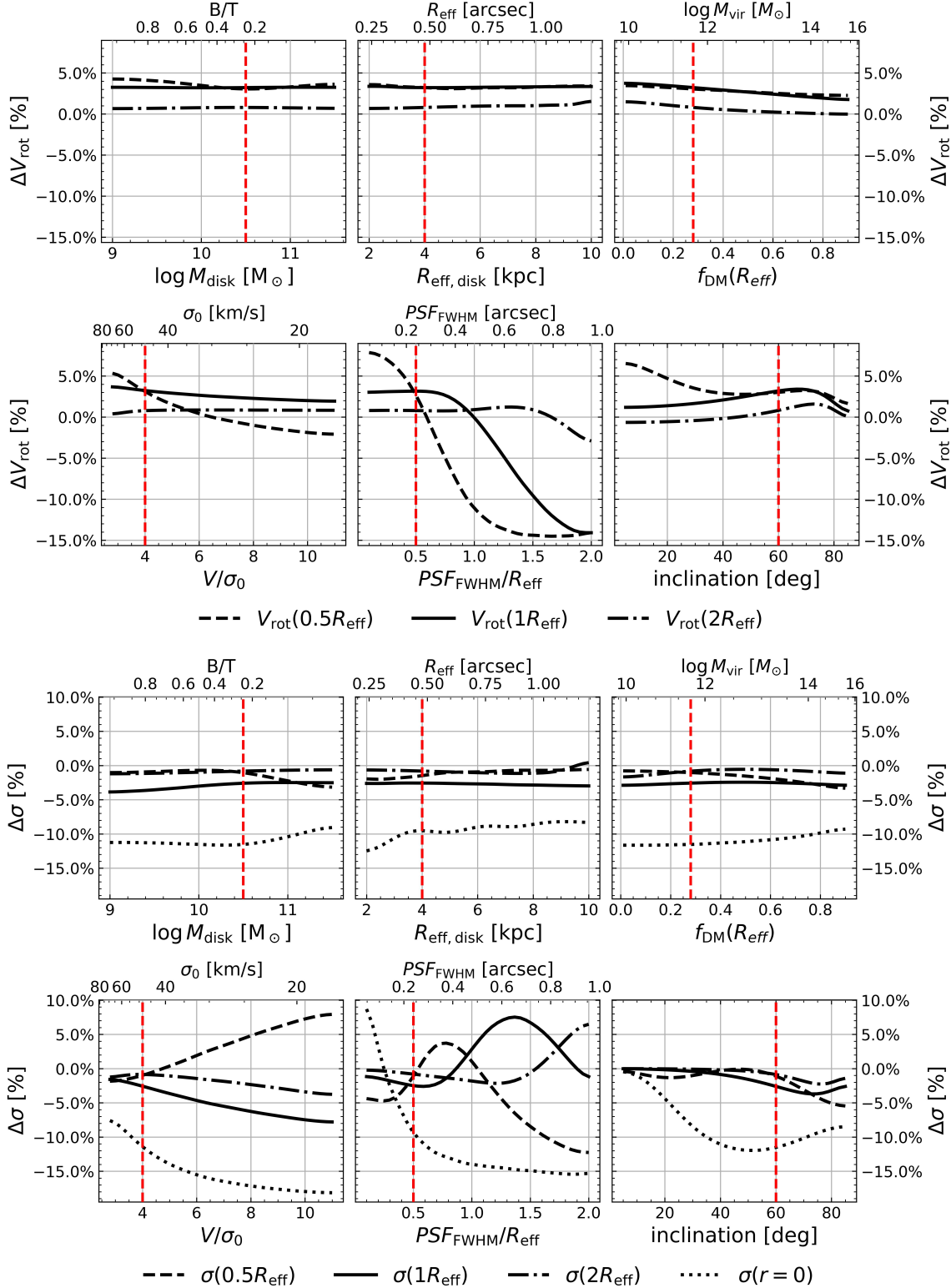


**Figure 4.** Comparison of the beam-smeared curves generated by `RotCurves` against `dysmalpy` for variations in key model parameters. Each panel shows the residual rotation velocity (top figure) or the residual velocity dispersion (bottom figure), defined as  $\Delta \equiv (\text{RotCurves} - \text{dysmalpy}) / \text{dysmalpy}$ , at notable apertures:  $r = (0.5, 1, 2) \times R_{\text{eff}}$  given by the dashed, solid, and dash-dotted lines respectively (in addition the the center  $r = 0$  for the dispersion, shown as a dotted.). The fiducial value given by the red dashed line. From top left to bottom right, the parameters are: Disk mass  $M_{\text{disk}}$ , bulge mass  $M_{\text{bulge}}$ , dark matter fractions at the effective radius  $f_{\text{DM}}(R_{\text{eff}})$ , v-over-sigma ratio  $V/\sigma_0$ , FWHM of the circular PSF in units of the effective radius,  $PSF_{\text{FWHM}}/R_{\text{eff}}$ , and the inclination angle  $i$ .

(e.g., mass) or a strong beam-smearing effect (e.g., PSF size). Non-normalized versions of these plots can be found in Appendix A.

The velocity residuals at all apertures are within  $\lesssim 5\%$  with almost no dependence on the value of the parameter, except for PSF size. It is not surprising that the beam size has a strong effect, as it directly determines the mixing within the beam. Moreover, the inner aperture ( $0.5 \times R_{\text{eff}}$ ) is more susceptible to changes in the beam size, either when it is smaller than  $\lesssim 0.2 \times R_{\text{eff}}$  for which the velocity is overestimated, or when  $\text{PSF}_{\text{FWHM}} \gtrsim R_{\text{eff}}$  for which the inner velocity is underestimated. This can be easily understood by considering the area the beam covers. When the PSF FWHM is larger than the distance to the center, the beam collects velocities with opposite signs (i.e., the “blue” or “red” sides), and by going off the midplane it reduces the radial distance of these particles along the line of sight. For this reason,  $\Delta V_{\text{rot}}$  decreases with the beam size, and changes sign roughly when the  $\text{PSF}_{\text{FWHM}}$  matches the distance of the aperture from the center.

The velocity dispersions show a very similar behavior, with residuals of  $\lesssim 5\%$  at all apertures for almost the entire range of parameters considered, and even  $\lesssim 2\%$  for large parts (see Figure 4). In general, RotCurves will tend to underestimate the velocity dispersion by design, as it considers only the midplane and mixes fewer regions in its beam. This is shown by the strong trends in the bottom-middle panel of Figure 4. Importantly, there are two locations where the velocity dispersion has great significance: at the outskirts, where the velocity dispersion is less susceptible to beam-smearing, and at the center, where the dispersion is a sensitive probe of the central mass concentration. The residuals at the outer parts are very small,  $|\Delta\sigma(2R_{\text{eff}})| < 3\%$  (dot-dashed line in Figure 4), yet in the center the velocity dispersion is underestimated on average by  $\Delta\sigma(r = 0) \approx -10\%$  and up to 20% in extreme cases (dotted line). As discussed later, when fitting a model for given data points, RotCurves will typically find higher bulge masses than dysmalpy to compensate for the difference, as long as the uncertainties on the central data points are smaller than the residuals discussed here.

### 3.3 Fitting a rotation curve

To test how well RotCurves can recover the intrinsic model parameters, in the following section we construct a rotation curve using dysmalpy that we use as a “data” input for RotCurves with the fiducial model as our baseline. We sample the rotation curve out to  $3R_{\text{eff,disk}}$  at each half-width half-maximum (HWHM) of the PSF, and assume a flat uncertainty of 5%. Our model consists of five free physical parameters ( $M_{\text{baryon}}$ ,  $B/T$ ,  $R_{\text{eff,disk}}$ ,  $\sigma_0$  and  $M_{\text{vir}}$ ), with the rest fixed to their true values. While the inclination is often a source of known degeneracies with other parameters, such as the mass of the galaxy, we assume a fixed value in this analysis as it can typically be recovered from photometric isophote fitting. However, in the lowest resolution regime isophote fitting may become unreliable, especially when the beam is comparable to, or larger, than the minor axis. In such cases, it is best to treat the inclination as a free model parameter in RotCurves and constrain it using the prior distribution, e.g., as a truncated Gaussian, to correctly propagate the uncertainties. In our fiducial model we fix the inclination to its true value and use very relaxed prior probabilities for the free parameters, assuming uniform distribution for all parameters and draw randomized initial steps for each fitting procedure. We use an MCMC fitting procedure (see § 2.4) with 100 walkers and 3000 steps (of which 500 are discarded as burn-ins), suitable for autocorrelation times of  $\sim 70$  steps. The free parameters are initialized randomly centered around their true values and are free to vary with a uniform prior probability

Parameter	Prior	Model	RotCurves
$M_{\text{baryon}}$	Uniform	10.6	$10.75 \pm 0.13$
$B/T$	Uniform	0.25	$0.23 \pm 0.06$
$R_{\text{eff,disk}}$	Uniform	4	$5.4 \pm 0.8$
$\sigma_0$	Uniform	56	$49.0 \pm 1.1$
$M_{\text{vir}}$	Uniform	11.8	$11.1 \pm 0.6$

**Table 6.** Best fit values for the MCMC fitting using RotCurves for the fiducial model generated with dysmalpy. The value shown is the mean of the best fit values from  $n = 10$  separate fitting procedures, with the mean  $1\sigma$  uncertainty reported after the  $\pm$  sign. The statistical error is  $< 0.01\%$  the  $1\sigma$  for all parameters.

distribution. To test the robustness of the MCMC fitter, we perform  $n = 10$  separate fitting procedures with their own initial states, finding the statistical uncertainty  $\Delta_{\text{stat}} = \sigma/\sqrt{n}$  of the best fit values are an order-of-magnitude smaller than the uncertainties of the posterior itself.

The best fit values are given in Table 6 for both the median and maximum (MAP) of the posterior, and the rotation curves for the median values are shown in Figure 5, along with the MCMC corner plot. The resulting rotation and dispersion curves are an excellent fit and RotCurves recovers the model parameters well. The differences in the intrinsic rotation curve transform into slight systematics in the results of the fit: the effective radius of the disk is overestimated by almost a factor of 1.4, the baryon mass is slightly overestimated and the halo mass is lower than its true value. These are the result of RotCurves finding the combination of parameters that effectively minimize the differences of the two beam smearing procedures (see bottom of Figure 3). As such, there are some notable degeneracies between the parameters of the model. The bottom of Figure 5 shows the posterior distribution and covariances, from which we can see a degeneracy between the halo mass  $M_{\text{vir}}$  and both  $M_{\text{baryon}}$  and  $R_{\text{eff}}$ . This is understood when we consider how they affect one another – larger disk sizes result in RCs that fall further out, requiring less dark matter to reach similar velocities. The same goes with the baryon mass, as it simply scales the velocities higher.

Next, we vary each of the five main parameters of the model independently ( $\log M_{\text{disk}}$ ,  $\log M_{\text{bulge}}$ ,  $B/T$ ,  $R_{\text{eff,disk}}$ ,  $\sigma_0$ ,  $M_{\text{vir}}$ ) from the initial fiducial values, keeping the rest of the parameters fixed, and fit the data generate by dysmalpy as described previously. At each step we perform  $n_{\text{fits}} = 10$  independent MCMC fits and take the mean of the best fit median and best fit MAP, verifying the statistical uncertainties are negligible. Figure 6 shows the comparison for the RotCurves best fit median estimator. We can see that for a wide variety of parameters, RotCurves recovers the model parameters accurately, well within the confidence intervals of the MCMC fit. For brevity, we do not include the fitting results for all combinations, but some examples can be found in Appendix B. However, there is a strong systematic error for recovering the disk effective radius  $R_{\text{eff,disk}}$ , where RotCurves recovers higher values by a factor of  $\sim 1.5$ . This can be explained by looking at the velocity residuals in Figure 3, as differences in velocities are compensated by increasing the effective radius of the disk. For larger  $R_{\text{eff,disk}}$ , the velocity peaks further out, so the values obtained at the actual  $R_{\text{eff,disk}}^{\text{dysmalpy}}$  will match better. Another, weaker systematic is when the bulge dominates over the disk, i.e.  $M_{\text{disk}}/M_{\text{bulge}} \lesssim 0.3$ , and the disk mass is poorly inferred in such that RotCurves can not accurately probe below  $M_{\text{disk}}/M_{\text{bulge}} \approx 0.2$  (or  $B/T \gtrsim 0.8$ ).

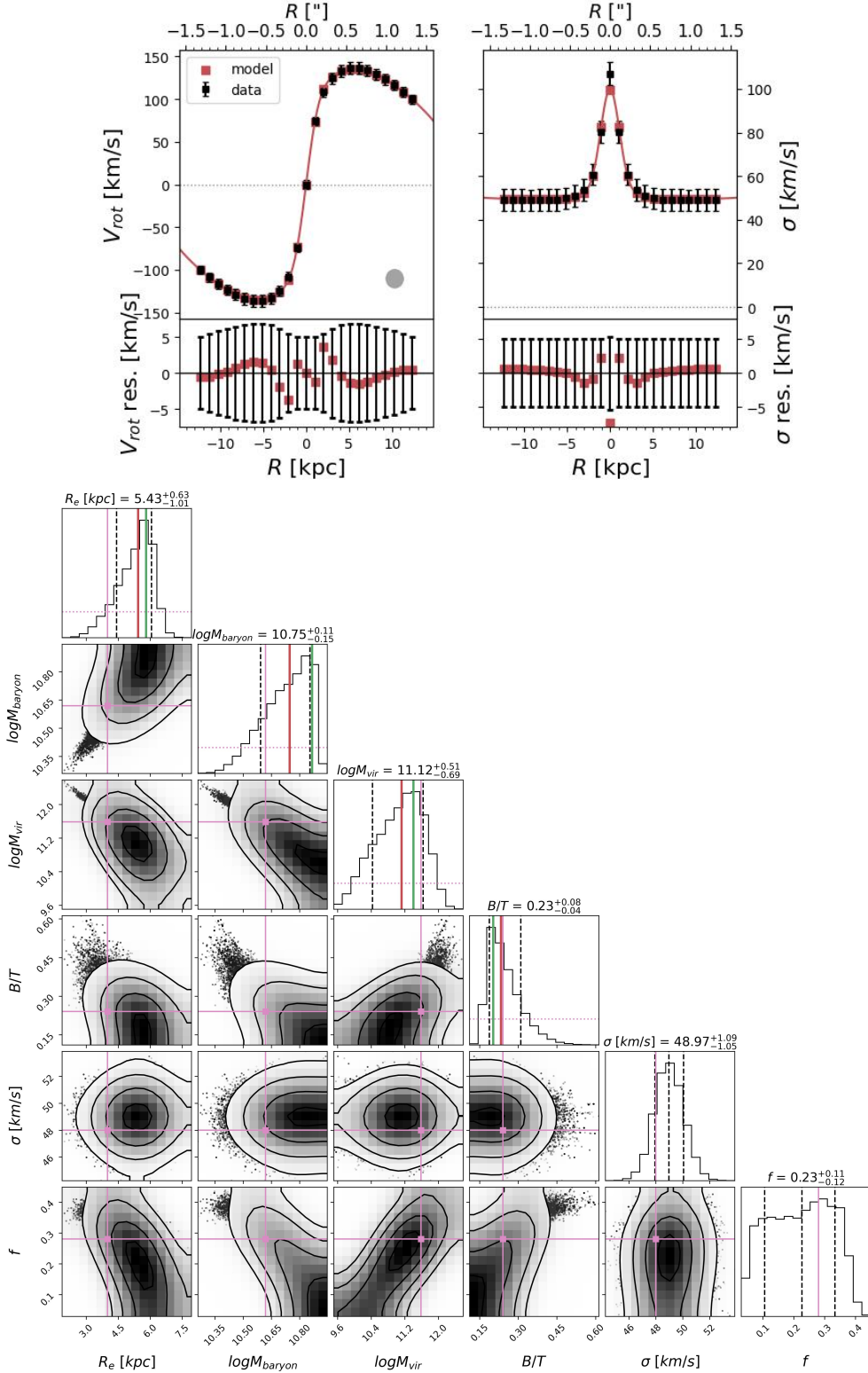


**Figure 5.** The best fit results for the fiducial model from the MCMC fitting procedure, fitted with `RotCurves` for a mock model created with `dysmalpy` up to 3 times the disk effective radius. Top figure: rotation curve (left) and velocity dispersion (right) with the `dysmalpy` mock model in black squares extracted in circular apertures given a PSF HWHM of  $0.25''$ , and the `RotCurves` best fit is shown in the red solid line. The residuals are shown in the bottom panels for a flat 5% uncertainty on the `dysmalpy` points for the purpose of the fit. Bottom figure: corresponding corner plot for the 5 fitted parameters:  $R_{\text{eff}}$ ,  $M_{\text{baryon}}$ ,  $M_{\text{vir}}$ ,  $B/T$ ,  $\sigma_0$  and the inferred dark matter fractions  $f_{\text{DM}}(R_{\text{eff}})$ . The median and MAP of the posterior is shown in the red and green lines, respectively, and the true value of the model in a pink line. The dashed lines show the 16<sup>th</sup> and 84<sup>th</sup> percentiles. The covariance panels show some degeneracies between the model parameters, namely between the halo mass and both baryon mass and disk size, or the halo mass and the B/T ratio.

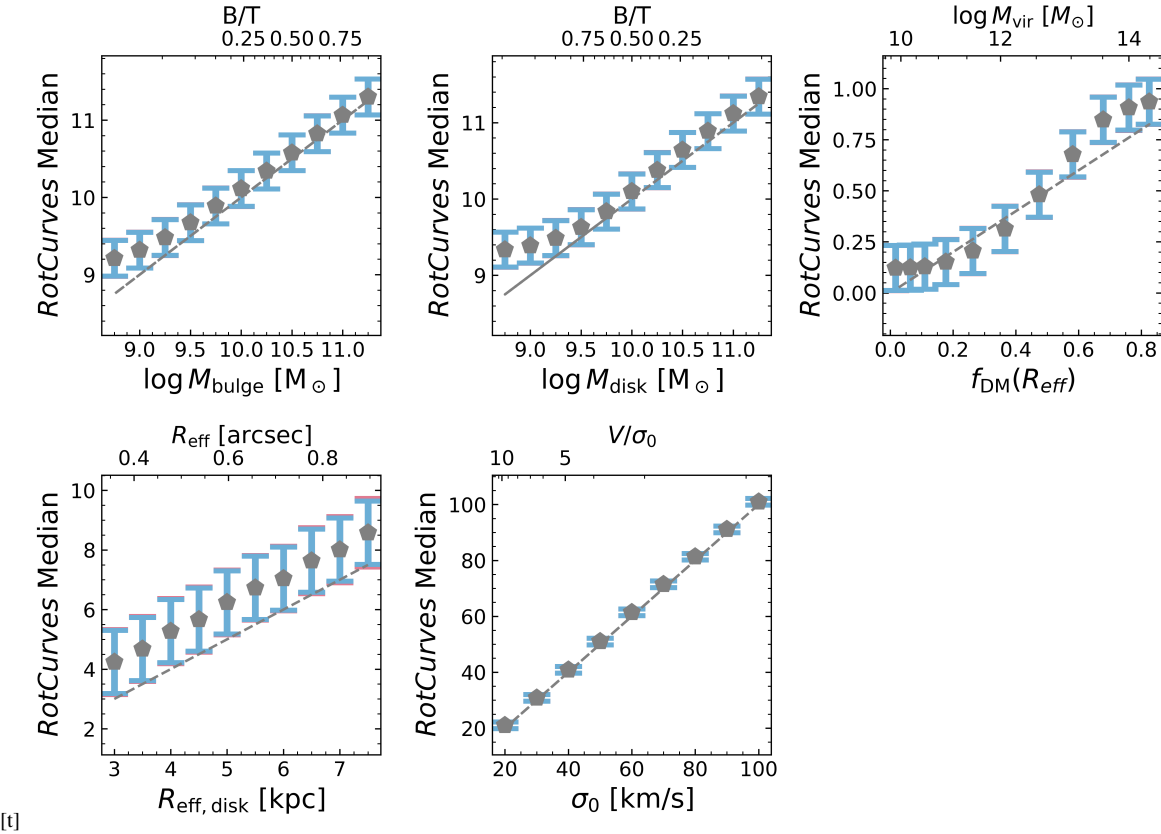


**Figure 6.** Model parameters inferred by RotCurves when fitting for a rotation curve created with `dysmalpy`. At each value the fit was run  $n_{\text{fits}} = 10$  separate times, and the pentagons show the mean of best fit value of these runs. The blue error bar marks the average MCMC confidence interval shown, and the dashed line is a one-to-one ratio. When significant, the statistical error  $\Delta_{\text{stat}} = \sigma_{\text{std}}/\sqrt{n_{\text{fits}}}$  is shown in an additional red error bar.

### 3.4 Effects of noise

To simulate more realistic data, we would need to consider how noise affects the mock-observed rotation curve from a given model. Because RotCurves does not input a full data cube, we cannot add noise in the underlying `dysmalpy` model without relying too heavily on the line fitting methods employed there. Instead, we adopt a simpler approach to achieve behavior similar to observed data, in which: (i) for smooth distributions the S/N follows the flux, peaking at the center and dropping with radius, (ii) the noise level  $\sigma_{\text{noise}}$  is spatially uniform, and (iii) the noise is drawn from a Gaussian distribution. Given that, we can reconstruct the emission line at a range of apertures,  $r_{\text{ap}}$ , separated by the size of the PSF FWHM, as pure Gaussian line profiles. The line centers,  $V_{\text{rot}}$ , and standard deviation,  $\sigma$ , are extracted from the `dysmalpy` modelling. The line is initially constructed with a fine spectral width of 10 km/s, then convolved over a Gaussian LSF and binned to a degraded spectral resolution  $\Delta v$ , mimicking the instrumental channel width, with an additional random phase of  $\Delta v/6$ . Next, as the noise-rms can vary slightly between spectral channels, we add a 10% variation of the noise level  $\sigma_{\text{noise}}$  in each channel, before drawing a Gaussian noise for each channel. Finally, the line profile is fitted with a Gaussian to recover the centroid velocity  $V_{\text{dys,noisie}}$  and velocity dispersion  $\sigma_{\text{dys,noise}}$ , at each aperture.

We set the S/N level as the ratio between the line peak and the noise standard deviation  $\sigma_{\text{noise}}$  at the effective radius  $R_{\text{eff,disk}}$ . The radial flux profile  $I_0(r_{\text{ap}})$  traces the mass of the disk (assuming M/L = 1 in the fiducial model), and so the line peak will drop exponentially

with radius, leading to higher S/N in the center and lower S/N as one goes outwards. If we normalize to the central flux, we simply get an exponential profile  $I_0(r) = e^{-r/R_d}$ . In that case, the S/N is:

$$\text{S/N} = \frac{I_0(R_{\text{eff,disk}})}{\sigma_{\text{noise}}} \approx \frac{0.186}{\sigma_{\text{noise}}} \quad (34)$$

where we used  $R_{\text{eff,disk}}/R_d = 1.68$  for an exponential disk. We define the limit of the observation as the point where the S/N drops below 3, which can be written as:

$$\begin{aligned} r_{\text{edge}} &= R_{\text{eff,disk}} \left[ 1 + \frac{1}{1.68} \ln \left( \frac{\text{S/N}}{3} \right) \right] \\ &\approx R_{\text{eff,disk}} \left[ 2 + \ln \left( \frac{\text{S/N}}{16} \right) \right] . \end{aligned}$$

At each S/N level we generate 10 individual mock-data, and fit each one using RotCurves, so we can average the random effects of the noise addition process.

Figures 7-8 show the results of an MCMC fitting for  $\text{S/N} = 25$  (and  $\Delta v = 35 \text{ km s}^{-1}$ ,  $\sigma_{\text{LSF}} = 30 \text{ km s}^{-1}$ ). The effect of the noise is clear on the mock data (black squared). At the outer RC, where the S/N is smaller, the line fitting becomes less secure and the uncertainties increase. The scatter in the mock data points to the centroid shifting around its “true” value, increasing as the S/N drops outwards. In the velocity dispersion, the width of the fitted line shifts more dramatically in the outer regions, even creating a completely artificial drop signature in one end. The best fit model generated with RotCurves is drawn in a red line, and the residuals show no clear systematic bias. The physical parameters are recovered well, albeit with large

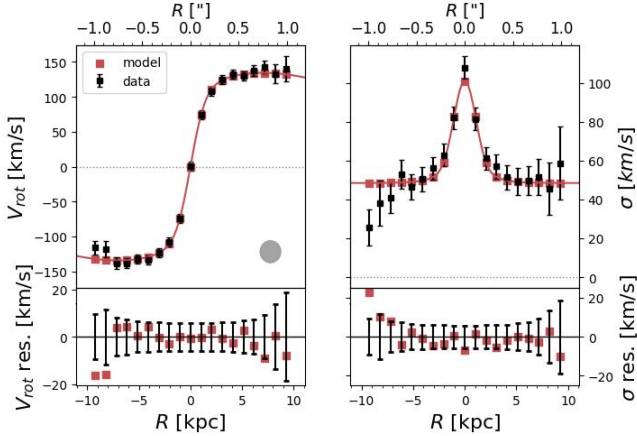


**Figure 7.** Results of the MCMC fit using `RotCurves` (red line, labeled “model”) to for data generated with `dysmalpy` included added noise with  $S/N = 25$ ,  $\Delta v = 35 \text{ km s}^{-1}$  and  $\sigma_{\text{LSF}} = 30 \text{ km s}^{-1}$  (black squares, labeled “data”), for our fiducial model. The deviation and uncertainty caused by the additional noise increase outwards, until they fall below  $S/N < 3$ .

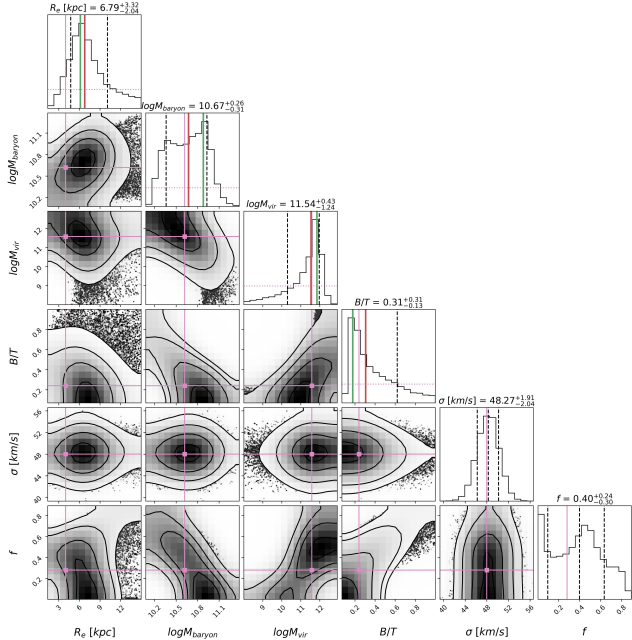


**Figure 8.** Corner of the MCMC fitting results for the fit shown in Figure 7, for  $S/N = 25$ ,  $\Delta v = 35 \text{ km s}^{-1}$ ,  $\sigma_{\text{LSF}} = 30 \text{ km s}^{-1}$ . The recovered parameters are recovered well given the posterior distribution, with  $B/T$  and  $f_{\text{DM}}$  showing a bias for overestimating the true value.

posterior uncertainties especially for  $M_{\text{baryon}}$ ,  $B/T$  and  $f_{\text{DM}}$ . This result is encouraging, as we have assumed no prior knowledge at all for the free parameters and let them vary freely in the parameter space. In real observations, some parameters can usually be constrained (e.g. baryonic mass from  $M_{\star}$ , the effective radius from imaging of the stellar continuum, or  $B/T$  ratios from aperture photometry) such that only smaller regions are explored and the posterior distribution becomes narrower.

We explore the trend on the parameter recovery based on  $S/N$  level in Figure 9. The line shows a running median and the shaded region

shows the statistical scatter over the 10 realizations at each  $S/N$  level. `RotCurves` improves with increasing  $S/N$  for all parameters, as more kinematic information is included as  $r_{\text{edge}}$  increases, with significant improvement at  $S/N > 25$ , until it converges at the intrinsic biases discussed in previous sections. Interestingly, the recovery of the bulge mass  $M_{\text{bulge}}$  and velocity dispersion  $\sigma_0$  are not sensitive to changes in  $S/N$ , as they can be well determined by the inner RC alone. Yet, as we already discussed earlier, the systematic overestimation of the bulge is evident and does not improve with higher  $S/N$ .

The parameters most affected are the disk mass  $M_{\text{disk}}$  and dark matter fractions  $f_{\text{DM}}(R_{\text{eff}})$ , with great improvements as  $S/N \gtrsim 25$  (corresponding to  $r_{\text{edge}} \gtrsim 2.3$ ). At high  $S/N \gtrsim 40$ , or  $r_{\text{edge}} \gtrsim 2.6$ , both of them are recovered very well, with no apparent systematic biases. Reaching far out into the RC is crucial for a reliable interpretation of the parameters, as in the low  $S/N$  regime the disk is underestimated by a factor  $\sim 0.5 - 0.7$  and the dark matter fraction (a proxy for the halo mass) is overestimated by  $\sim 1.5 - 2$ . Finally, the effective radius has only a slight improvement with  $S/N$ , with a clear systematic bias of larger disk sizes, by a factor of  $\sim 1.5$  (similar to the values discussed in § 2.4).

## 4 CONCLUSIONS

In this paper we presented `RotCurves`<sup>7</sup> as a tool to carry out rotation curve modelling, allowing for fast exploration of various assumptions on mass models. The primary goal of this work has been to test the performance of our beam smearing correction, performed by projecting the beam in the plane of the disk (see § 2.3), against the full 3D treatment performed by the code `dysmalpy`. We use `dysmalpy` as the choice for comparison as it is also a forward mass modelling tool, assuming analytical function for the mass components. Such benchmarking exercises are critical for ensuring reliability and reproducibility in kinematic studies, particularly as the field moves toward larger data sets from future IFU surveys. `RotCurves` created a beam-smeared rotation curve in a few 10ms, which is about 200 – 300 faster than `dysmalpy`. By systematically comparing the two codes under controlled conditions, we find small differences in the mock observed rotation curves, and show that `RotCurves` can recover well the intrinsic model parameters, even when including a more realistic noise signal. Performance is impacted negatively mostly for low  $S/N$  and large beam sizes.

We first compare the beam smearing treatment between `RotCurves` and `dysmalpy` for an identical model galaxy (the “fiducial model”), with typical values for a main sequence SFG at  $z = 2$ , and the galaxy is well resolved with a PSF FWHM of half an effective radius. We find that despite the methodological differences, both mock observed rotation curves agree to within 5% ( $\approx 7 \text{ km s}^{-1}$ ) across all radii. As expected, discrepancies are largest in the inner regions where the velocity gradients are steepest due to the presence of the bulge, and become smaller beyond the effective radius. The same is true for the velocity dispersion, where both approaches agree to within 5% ( $\approx 5 \text{ km s}^{-1}$ ), with the largest discrepancy in the center. Due to the 2D approach of `RotCurves`, the velocity dispersion is always under-estimated compared to `dysmalpy`, whereas the velocity difference varies. The PSF size has the greatest effect on the rotation curves, and as the system becomes less resolved differences are much larger, up to  $\approx 15\%$ . This is most notable in marginally resolved systems, when the PSF FWHM becomes larger than one

<sup>7</sup> <https://github.com/nestoramit/RotCurves>

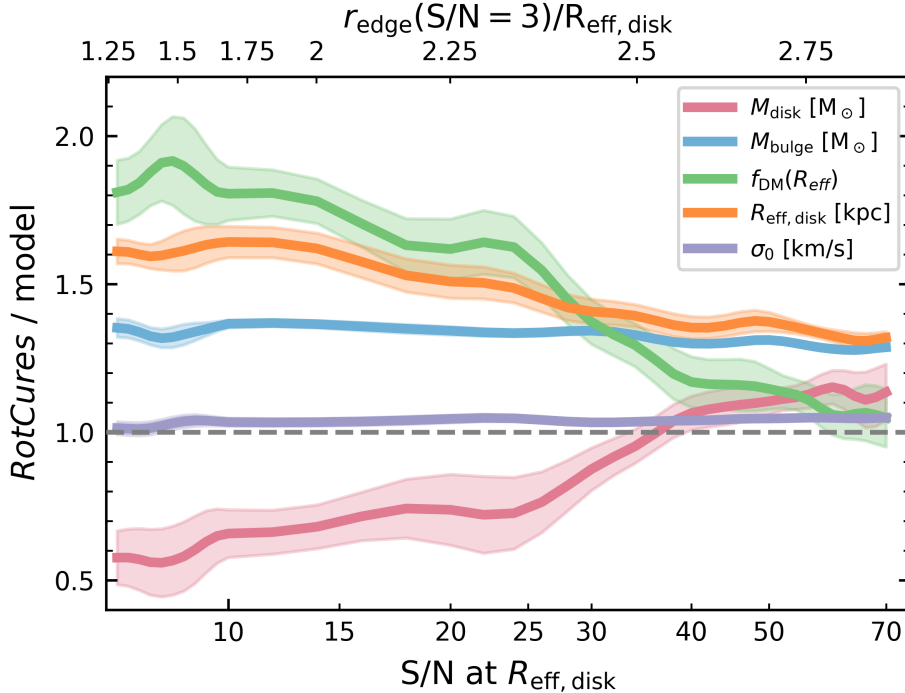


**Figure 9.** Best fit values obtained while fitting a mock-observed rotation curve created with `dysmalpy`, and fitted using the MCMC fitter with `RotCurves`. The y-axis shows the difference in each parameter  $X$  as  $\Delta X = X^{fit} / X^{model}$ . The S/N is defined by the ratio of the line peak to the noise level at the disk effective radius, and the edge of the mock-observation is where the S/N drops below 3. At higher S/N, the difference decreases as the mock RC probes the outer parts of the RC, better constraining the model parameters.

effective radius. Other parameters, such as changing the mass of the disk or the bulge, the DM fractions, intrinsic velocity dispersion or inclination have little effect on the residual values.

`RotCurve` recovers the intrinsic model parameters well for a mock-observed rotation curve generated with `dysmalpy`. We use an MCMC approach to recover the posterior distribution simultaneously for five model parameters: the total baryon mass  $M_{\text{baryon}}$ , the disk effective radius  $R_{\text{eff}}$ , the bulge-to-total ratio  $B/T$ , the dark matter fraction  $f_{\text{DM}}(R_{\text{eff}})$ , and the intrinsic velocity dispersion  $\sigma_0$ . We vary each parameter over a wide range of values (see figure 6), performing 10 individual fits for each value for a total of  $\sim 550$  individual runs over the entire parameter space. Each fitting procedure has 100 walkers and 3000 steps (of which 500 are burn-in steps), which is  $\approx 40 - 50$  times the autocorrelation time, and assuming uniform priors and randomized initial phases at each run. The fit procedure is robust, as the best fit values have very little scatter and negligible statistical errors. The posterior distribution uncertainty is significant, but the recovered median (and maximum a-posteriori, MAP) values are in very good agreement with the intrinsic values. However, the disk effective radius was systematically inferred to be larger ( $\approx 50\%$ ), and well outside the  $1\sigma$  uncertainty for  $R_{\text{eff}} > 6$  kpc. Similarly, the fit increasingly misses for disk masses below  $M_{\text{disk}} < 10^{9.5} M_{\odot}$ , overestimating the disk mass by  $\approx 10\%$ . Yet, overall, `RotCurves` can accurately recover the intrinsic parameters for a wide range in mass models.

Finally, we test the performance of `RotCurves` under realistic observational conditions by including a line spread function and adding Gaussian noise to the `dysmalpy`-generated velocity maps at levels typical of current IFU surveys (see figure 9). We explore signal-to-noise ratios ranging from S/N = 5 – 70, that we define by

the peak flux over a beam element centered at the effective radius. At each S/N level we generate a mock-data from `dysmalpy` which we fit using `RotCurves`. At high S/N the recovered values are in excellent agreement with the intrinsic parameters, with the same intrinsic biases discussed earlier, and as the S/N drop we start seeing larger discrepancies. The bulge mass  $M_{\text{bulge}}$  and velocity dispersion  $\sigma_0$  have almost no dependency on S/N, whereas the disk mass  $M_{\text{disk}}$ , DM fractions  $f_{\text{DM}}(R_{\text{eff}})$  and effective radius  $R_{\text{eff}}$  start to deviate as  $S/N \lesssim 25$ . However, even at very low S/N we recover reasonable values that can be used as an estimate. These results demonstrate that `RotCurves` can perform reliably for the majority of observations, but we advise to be cautious when interpreting results from poorly resolved, low S/N systems - a regime that is unfortunately common in high-redshift studies.

Looking forward, `RotCurves` is designed to serve multiple roles in the analysis of galaxy kinematics. As an exploratory tool, it enables rapid testing of different mass model assumptions—such as varying dark matter profiles, baryon distributions, or including/excluding bulge components—without the computational overhead of full 3D modeling. This makes it particularly useful in the early stages of analysis when the appropriate model complexity is not yet clear, or when investigating systematic effects from different modeling choices. For real observational data, `RotCurves` can provide quick parameter estimates and identify potential issues (e.g., warps, asymmetries, or kinematic substructure) before committing to more computationally expensive fitting procedures. Perhaps most critically, as we enter the era of large ground-based IFU surveys (e.g., VLT/MAVIS) or space telescopes (e.g. JWST/NIRSpec), and next generation ground-based instruments (e.g., ELT/MOSAIC, GMT IFS), computational efficiency will become essential to effectively analyze the data. The

ability to process large samples with consistent methodology, while maintaining the flexibility to adapt models to different mass regimes and redshifts, positions `RotCurves` as a valuable tool for future statistical studies of galaxy dynamics and evolution. The code is publicly available on [github](https://github.com/nestoramit/RotCurves).

## ACKNOWLEDGEMENTS

We thank the referee for their insightful comments and helpful suggestions. ANS and AS are supported by the Center for Computational Astrophysics (CCA) of the Flatiron Institute, and the Mathematics and Science Division of the Simons Foundation, USA. We thank the German Science Foundation (DFG) for support via German-Israel Project (DIP) grant STE/1869-2 GE 625/17-1. HÜ acknowledges funding by the European Union (ERC APEX, 101164796). NMFS, CB, GT, JMES and JC acknowledge funding by the European Union (ERC Advanced Grant GALPHYS, 101055023). Views and opinions expressed are, however, those of the authors only and do not necessarily reflect those of the European Union or the European Research Council. Neither the European Union nor the granting authority can be held responsible for them.

## DATA AVAILABILITY

No new data were generated or analysed in support of this research. The software described in this paper is publicly available at <https://github.com/nestoramit/RotCurves>.

## SOFTWARE

This paper makes use of the publicly available PYTHON packages: `scipy` (Virtanen et al. 2020), `numpy` van der Walt et al. (2011), `matplotlib` (Hunter 2007), `seaborn` (Waskom 2021), `emcee` (Foreman-Mackey et al. 2013b), `corner` (Foreman-Mackey 2016) `pandas` (The pandas development Team 2024), `Astropy` (Astropy Collaboration et al. 2013, 2018, 2022) and `dynamalpy` (Davies et al. 2004a,b; Davies et al. 2011; Cresci et al. 2009; Wuyts et al. 2016; Lang et al. 2017; Price et al. 2021; Lee et al. 2025b).

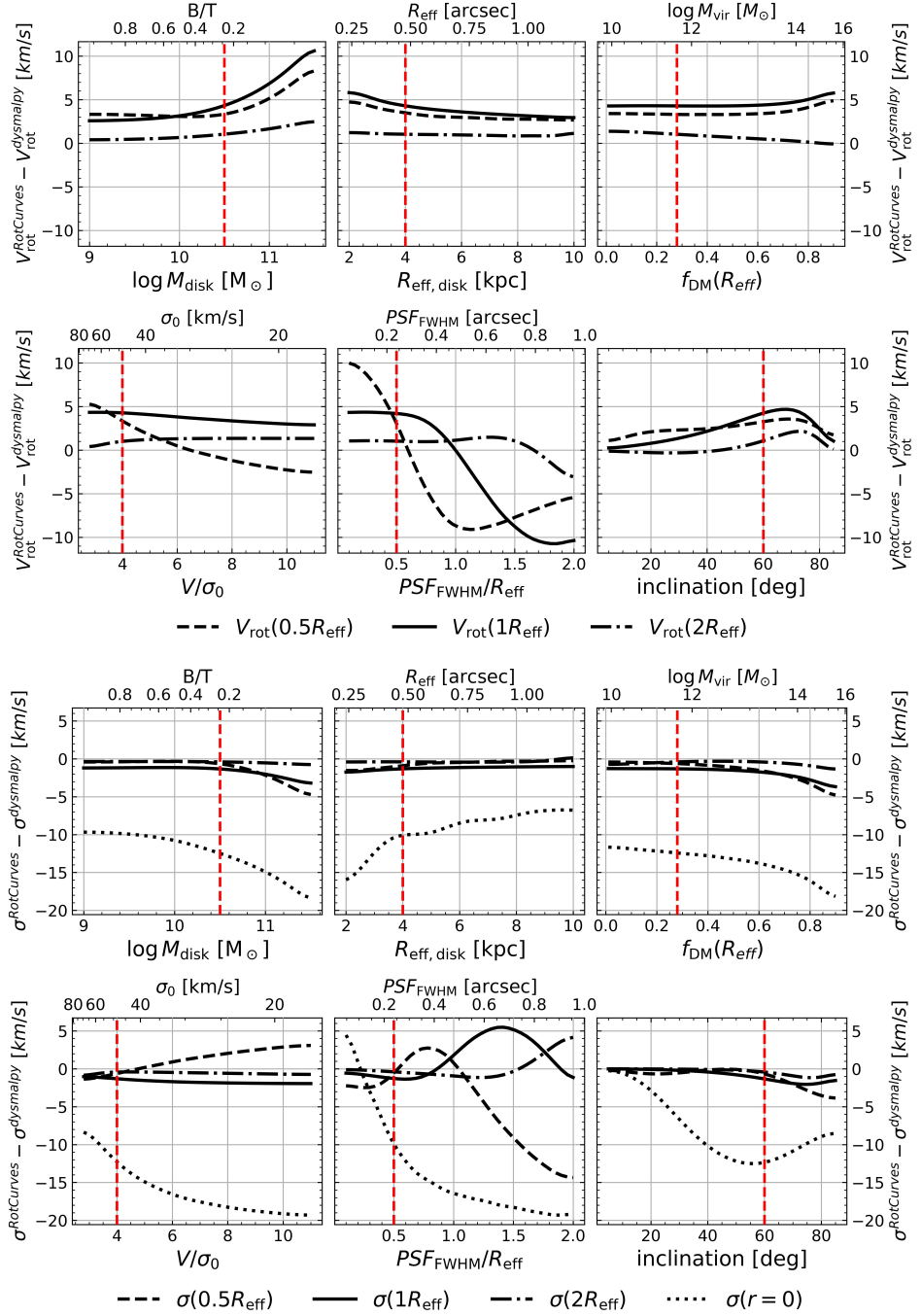


Figure A1. Same as Figure 4 but with residuals in physical units of km/s.

## APPENDIX A: RESIDUALS FOR BEAM SMEARING COMPARISON IN PHYSICAL UNITS

Following the discussion in section § 3.1, Figure A1 presents the residuals between the beam-smeared rotation curves as a function of model parameters in absolute terms, without normalizing by the dysmalpy values (as is done in Figure 4).

**APPENDIX B: FIT RESULTS FOR VARIOUS PARAMETER COMBINATIONS**

Following section 3.2, we performed variations in the model parameters and examined the results of the MCMC fit of RotCurves. Figure 6 shows the comparison between the best fit and the true values. Each combination was fit with 10 MCMC fitting procedures, resulting in a large number of figures. In the following appendix, we present some representative fitting results allowing to examine the degeneracies and residuals for some of these cases in Figures B1-B5. In all cases, the fiducial parameters describe the true values of the model, except for the parameter explicitly written in the figure caption, noting its value.

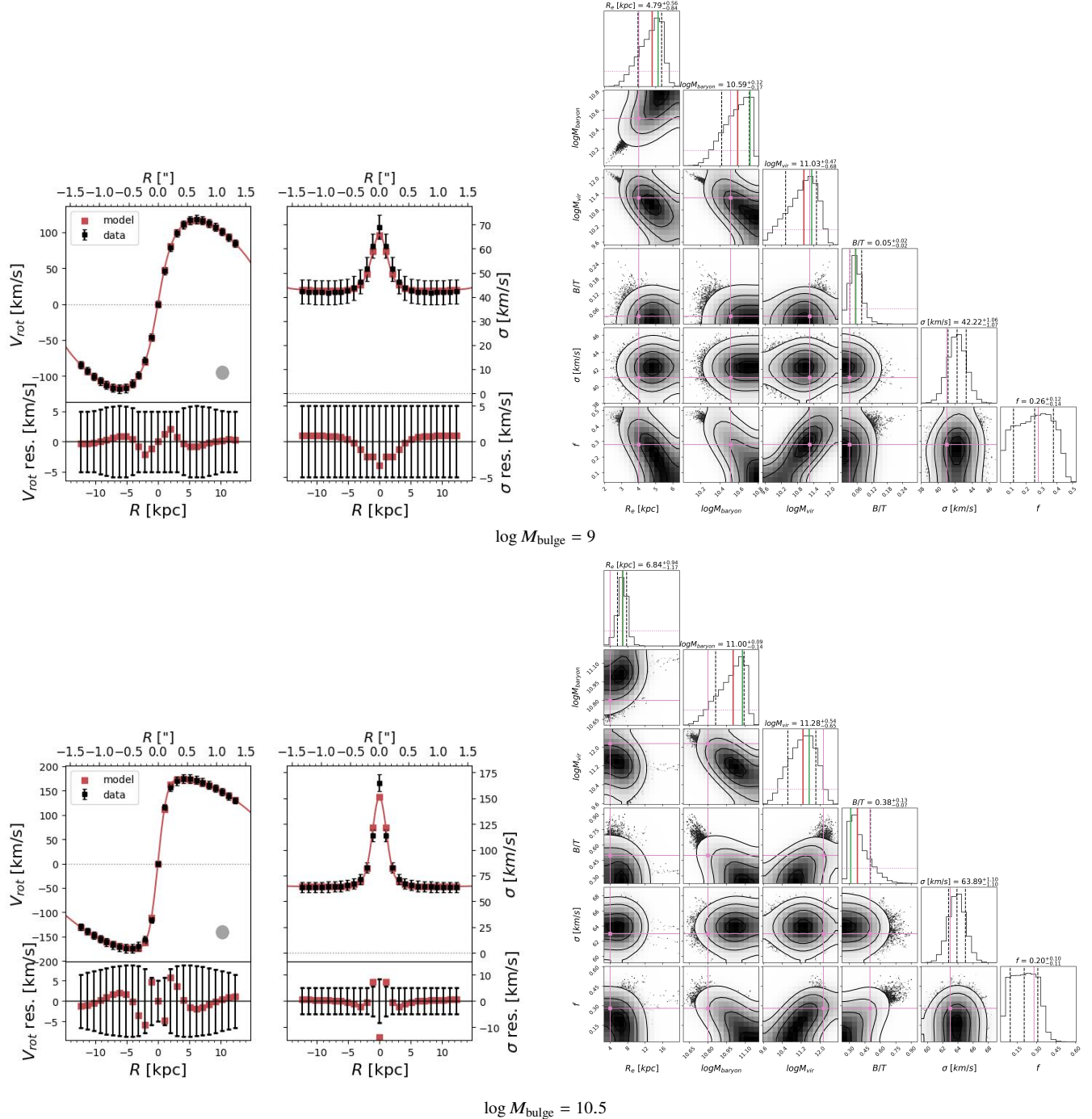


**Figure B1.** Two variation in bulge mass for the MCMC fit results with RotCurves on a model generated by dysmalpy.

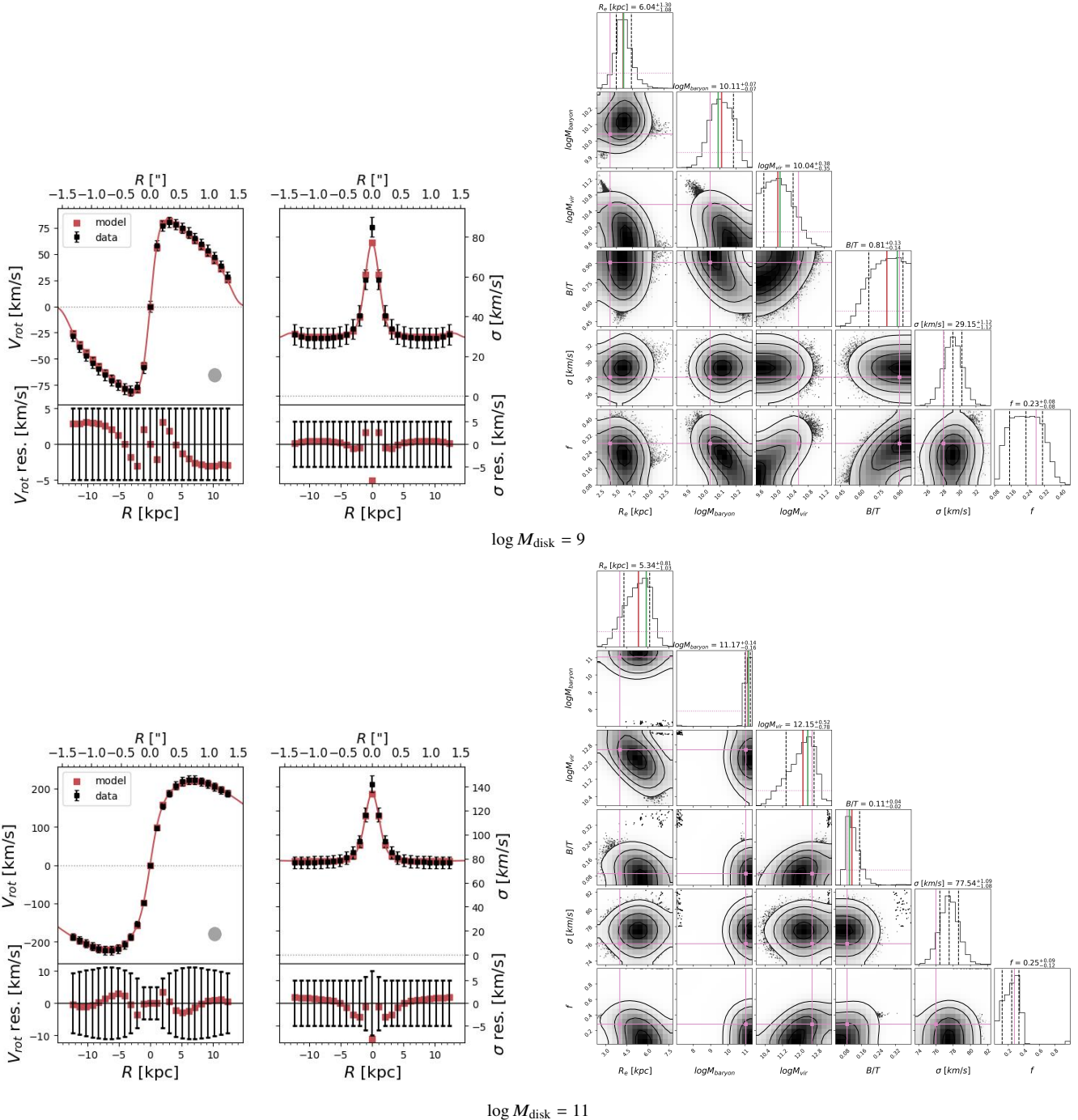


**Figure B2.** Two variation in disk mass for the MCMC fit results with *RotCurves* on a model generated by *dysmalpy*.

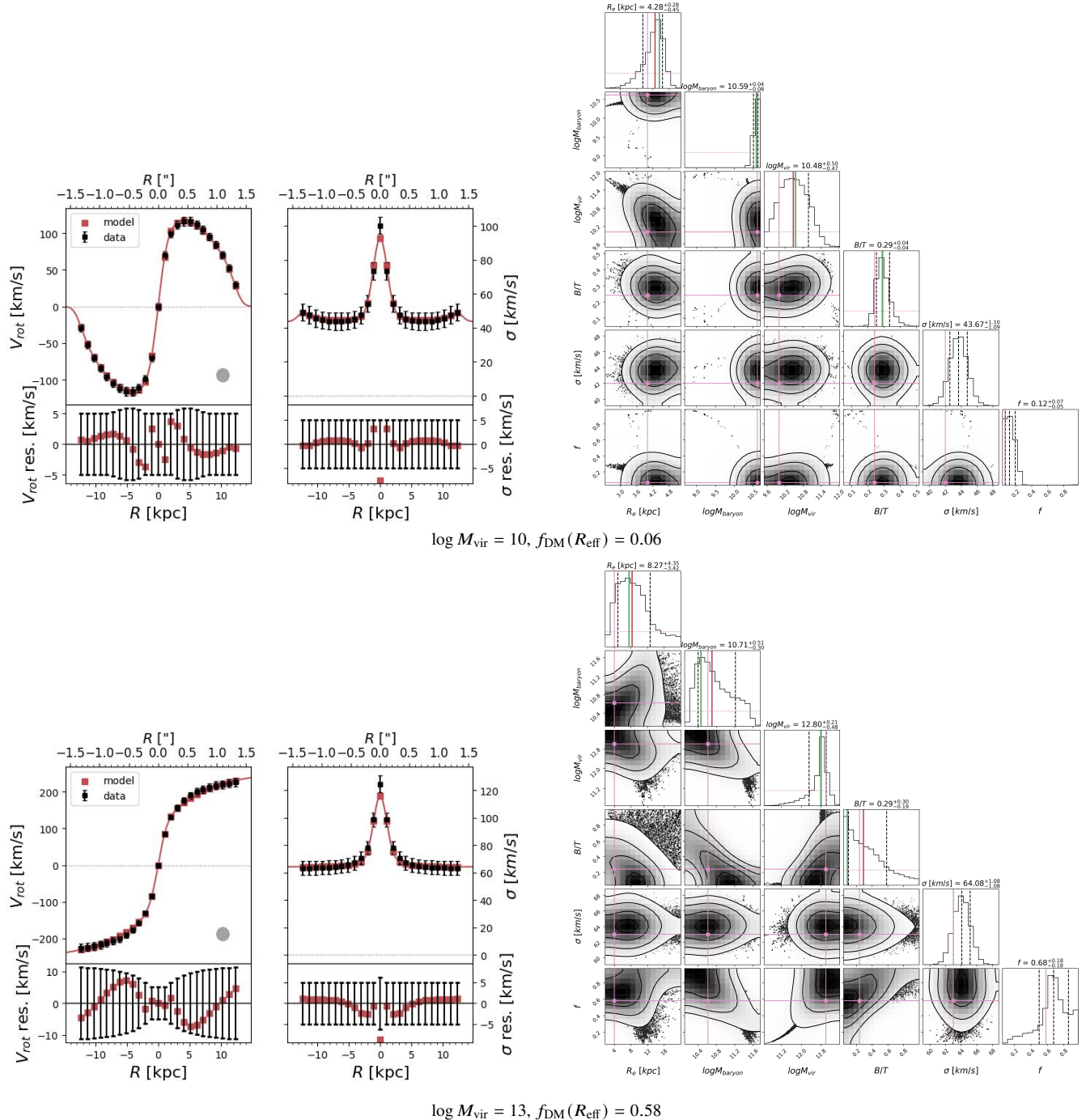


**Figure B3.** Two variation in halo mass for the MCMC fit results with RotCurves on a model generated by `dysmalpy`.

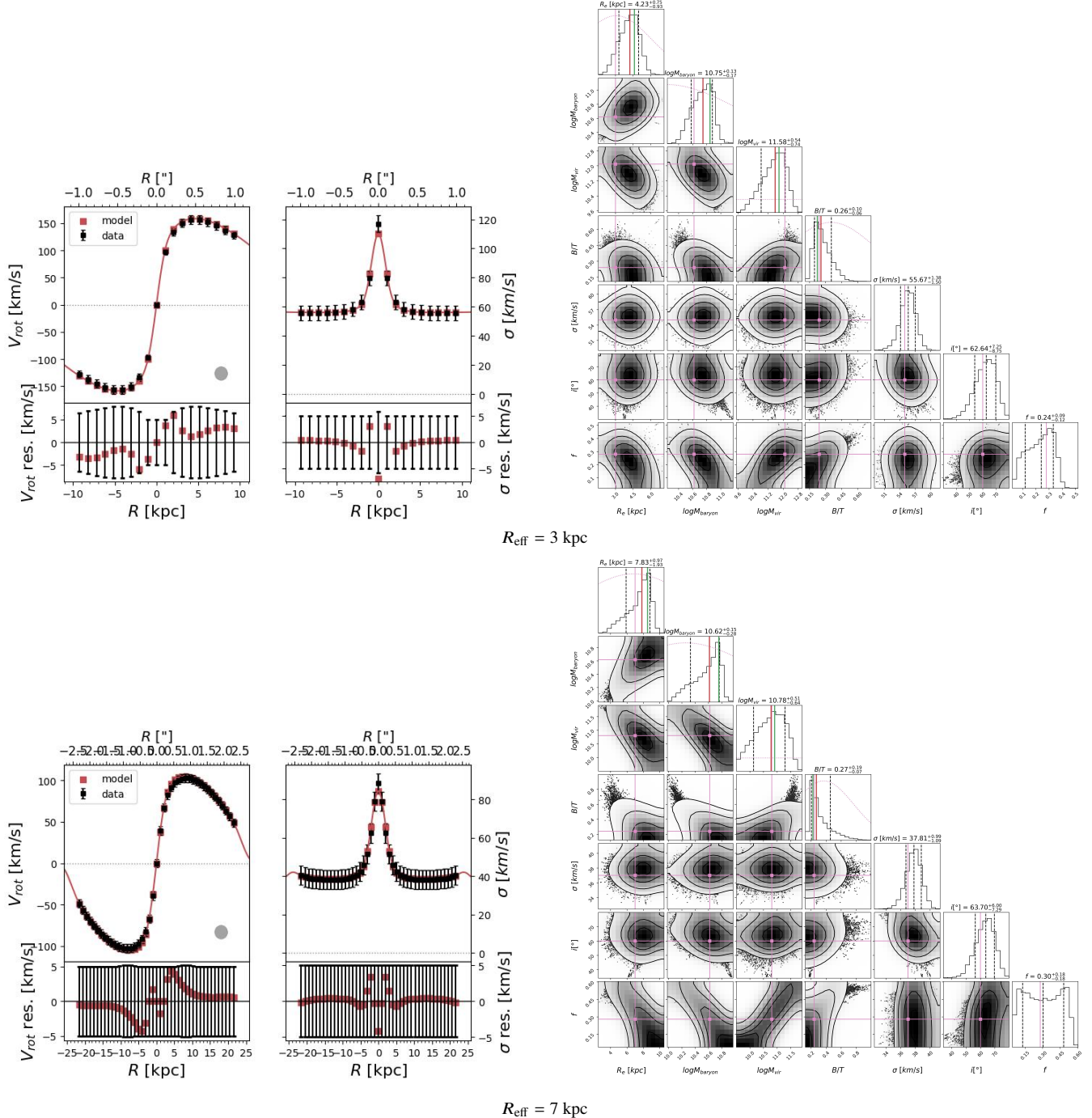


**Figure B4.** Two variation in the disk effective radius for the MCMC fit results with RotCurves on a model generated by dysmalpy.

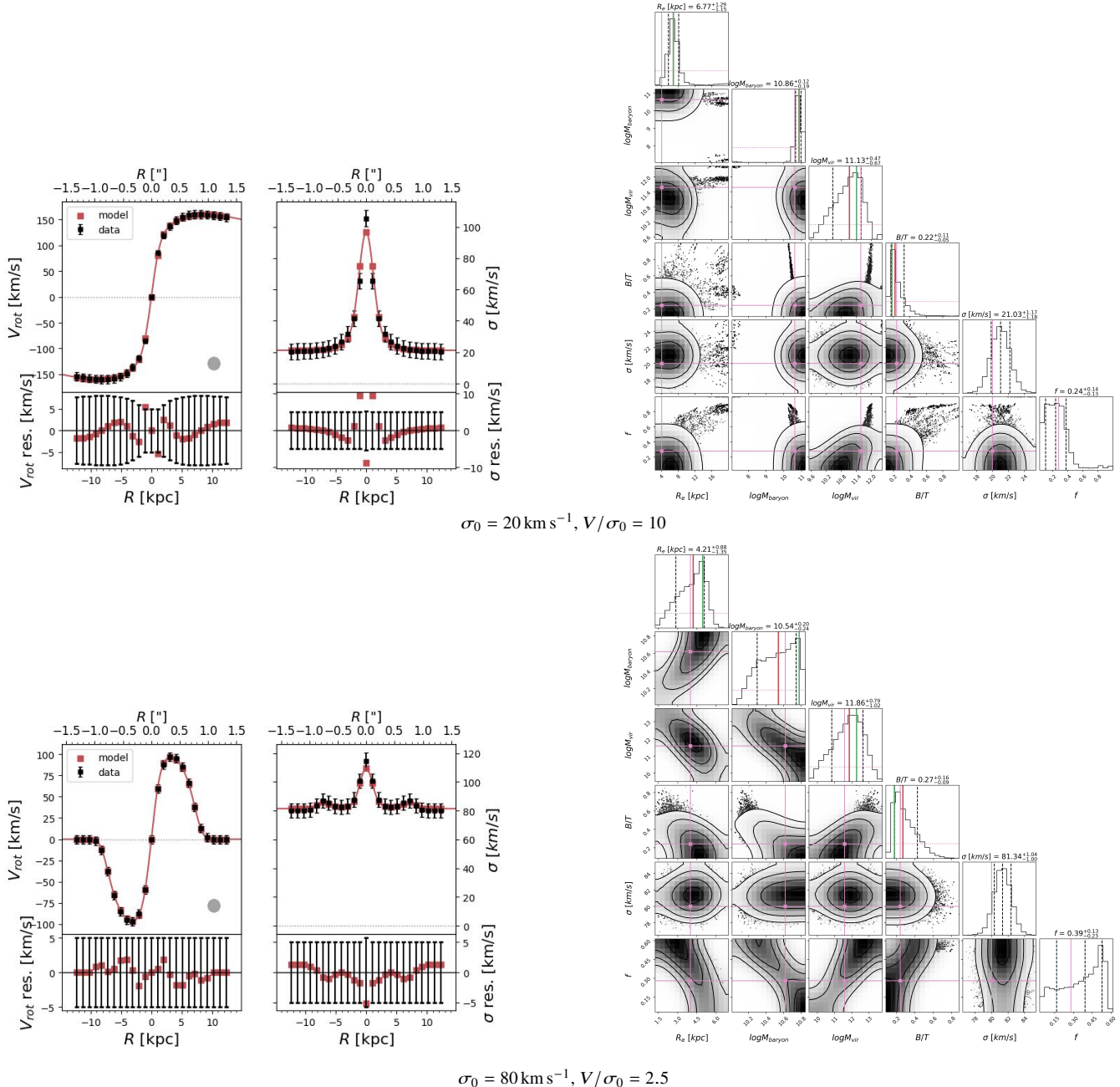


**Figure B5.** Two variation in the intrinsic velocity dispersion for the MCMC fit results with RotCurves on a model generated by dysmalpy. At very high  $\sigma_0$ , the rotation curve of our idealized axisymmetric model falls extremely rapidly and loses the information contained in the outer RC about the dark matter content, resulting in a close to flat posterior on  $f_{\text{DM}}$ .

## APPENDIX C: MOCK OBSERVATION AND NOISE

In section 3.4 we discuss the procedure for adding noise to a rotation curve calculated with `RotCurves`, defined by the S/N ratio of the line peak at the effective radius  $R_{\text{eff}}$ , with a given spectral list-spread-function (LSF) and a channel resolution of  $\Delta\nu$ . Figure 9 show the how the recovery of `RotCurves` improves as a function of the S/N, given the systematics discussed in the paper. We show two cases of the process of generating the noise and the mock data points, and the consequent results of the MCMC fitting with `RotCurves`. Figure C1-C2 show the results for a low S/N of 10, and Figure C3-C4 for a high S/N of 70. As the edge of the mock data points depends on the S/N, as well as the lower uncertainties, it is clear to see the recovery of the physical parameters is much better in the high S/N regime.

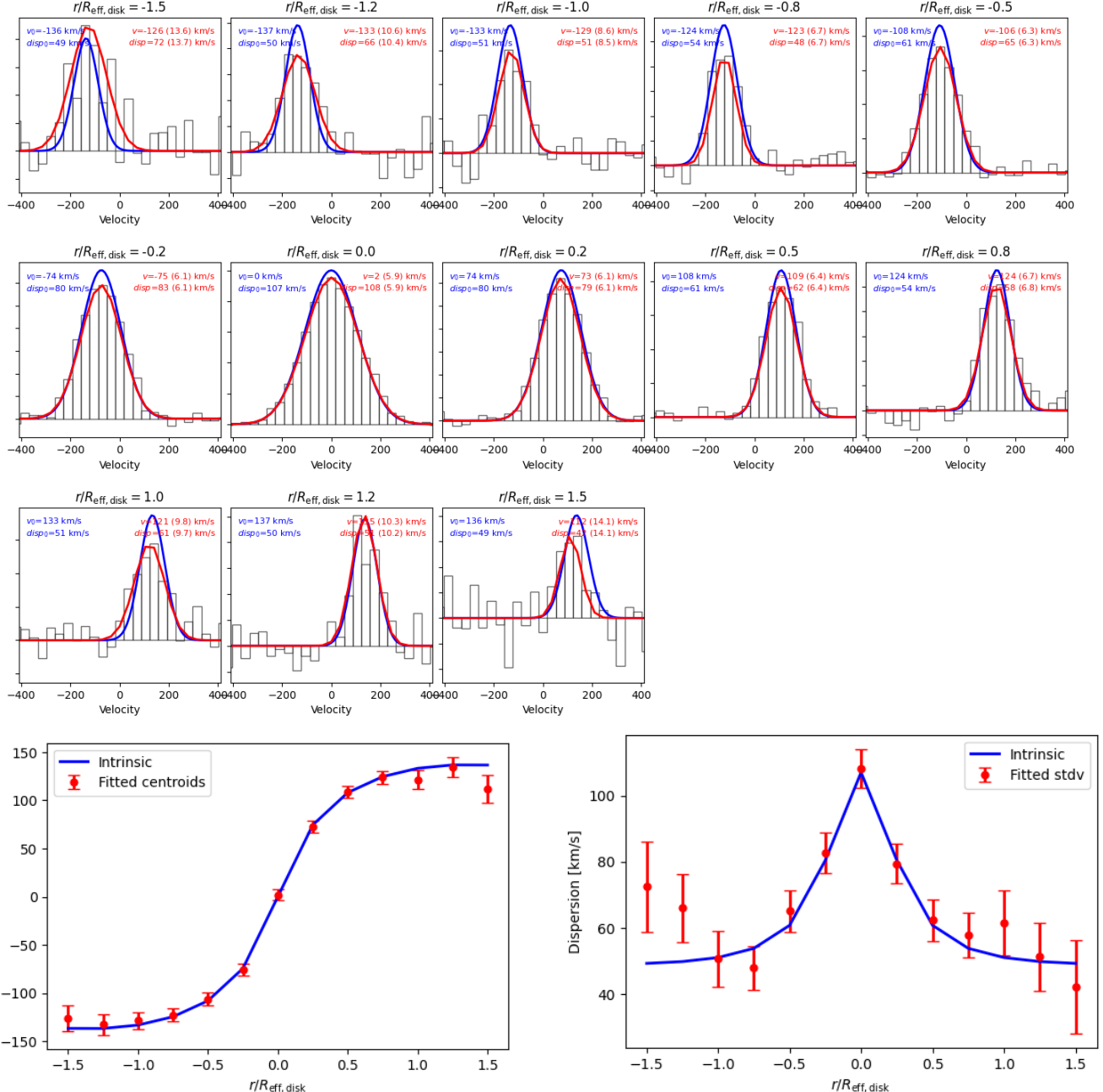


**Figure C1.** Mock observation process for a S/N of 10 at  $R_{\text{eff}}$ , a channel width of  $\Delta v = 35 \text{ km/s}$  and with a Gaussian LSF with  $\sigma_{\text{rmLSF}} = 30 \text{ km/s}$ . The emission lines are constructed from a pure Gaussian with ( $V_{\text{rot}}$ ,  $\sigma$ , in blue) taken from `dysmalpy`, with a M/L following the exponential disk. The line is convolved and binned over the LSF, then added a noise level drawn from a Gaussian distribution. The noisy emission line is fitted with a Gaussian (red line), which is used as the mock data points in the rotation curve (middle panel) and dispersion curve (bottom panel) for the MCMC fitting with `RotCurves`.

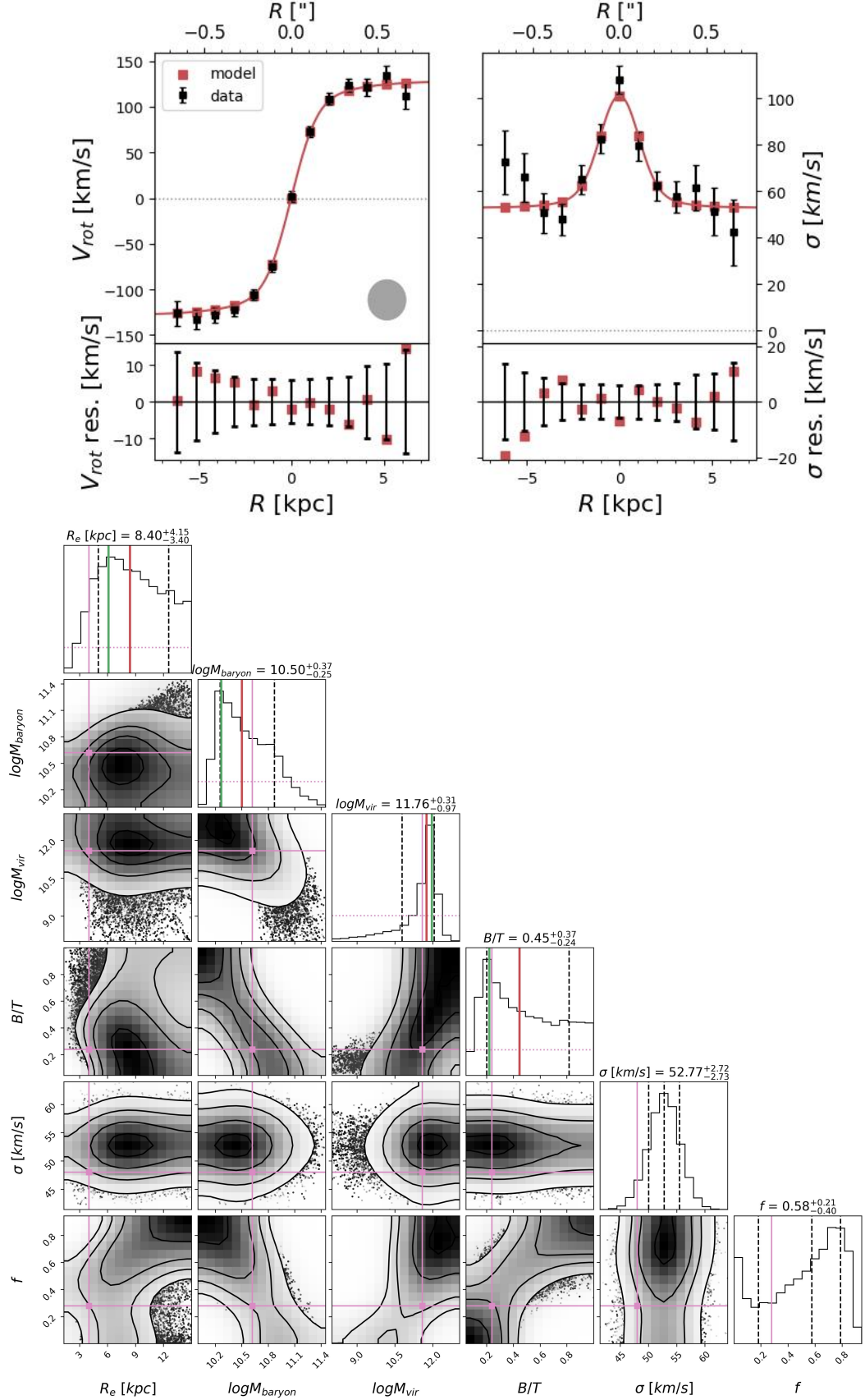


**Figure C2.** Results of the MCMC fit for a mock observation with a S/N of 10 at  $R_{\text{eff}}$ , given in Figure C1.

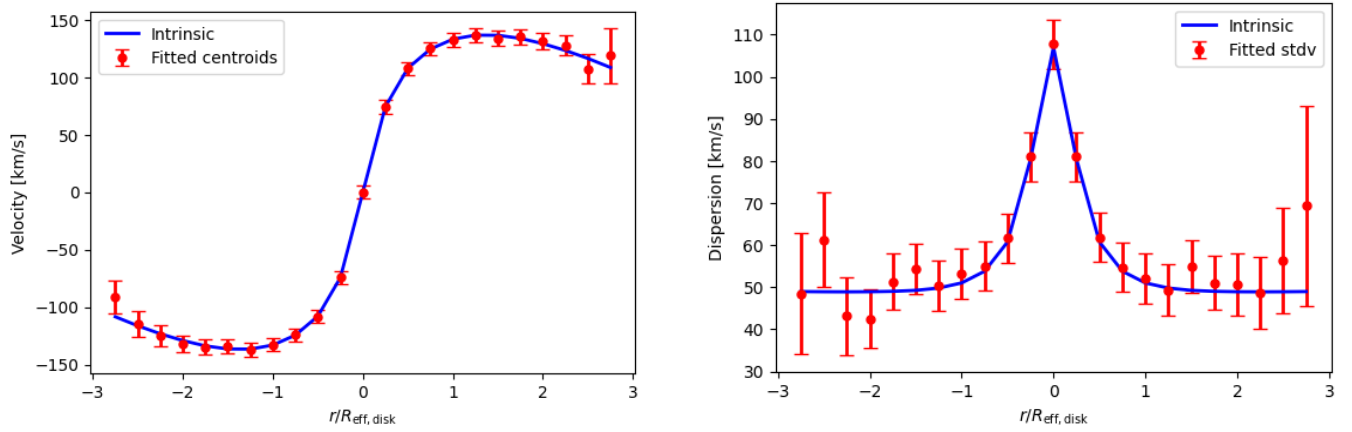
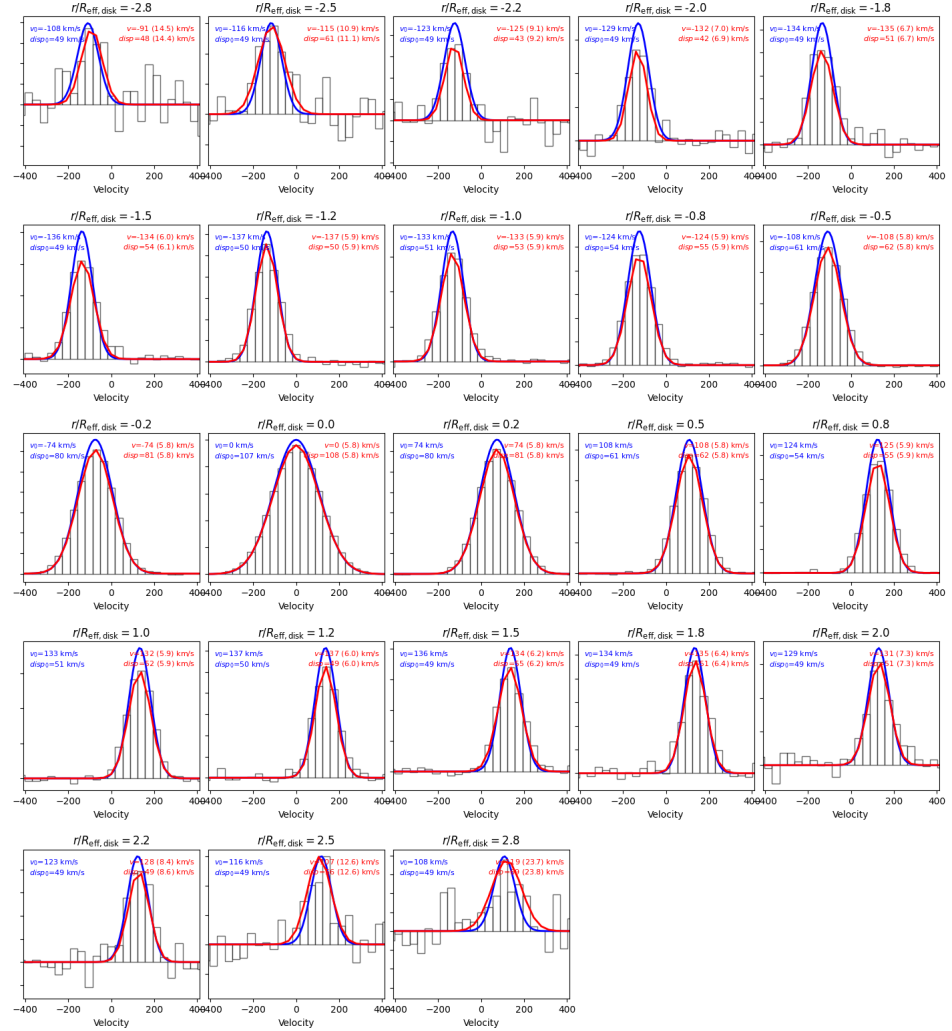
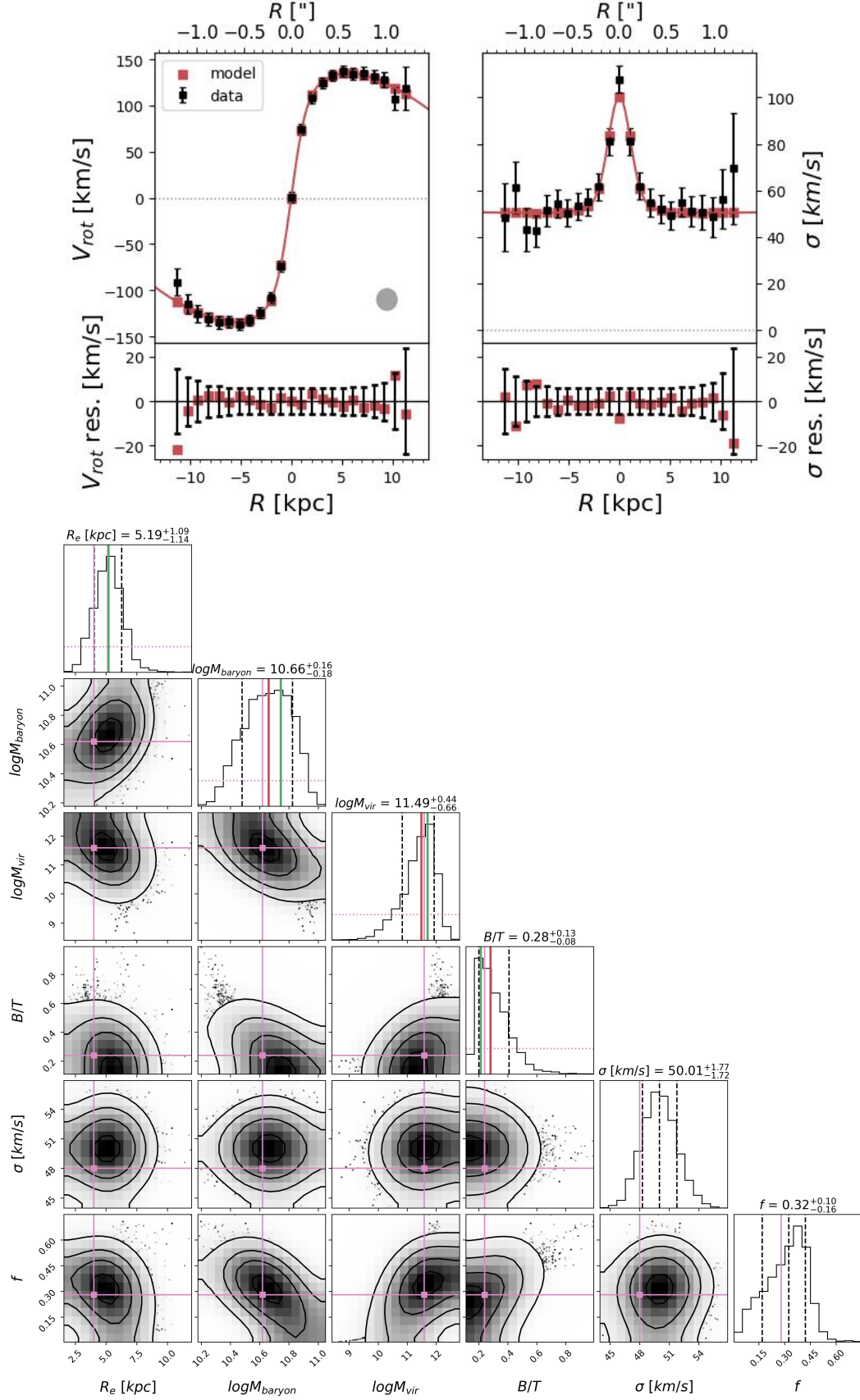


Figure C3. Same as C1, but for a S/N of 70 at  $R_{\text{eff}}$ .



**Figure C4.** Results of the MCMC fit for a mock observation with a S/N of 70 at  $R_{\text{eff}}$ , given in Figure C3.

## REFERENCES

Abdurro'uf et al., 2022, *ApJS*, **259**, 35

Akins H. B., et al., 2025, *arXiv e-prints*, p. arXiv:2508.06607

Astropy Collaboration et al., 2013, *A&A*, **558**, A33

Astropy Collaboration et al., 2018, *AJ*, **156**, 123

Astropy Collaboration et al., 2022, *ApJ*, **935**, 167

Bacon R., et al., 2015, *A&A*, **575**, A75

Barišić I., et al., 2025, *ApJ*, **983**, 139

Bertola E., et al., 2025, *A&A*, **699**, A220

Bewketu Belete A., et al., 2021, *A&A*, **654**, A24

Binney J., Tremaine S., 2008, Galactic Dynamics: Second Edition

Birkin J. E., et al., 2024, *MNRAS*, **531**, 61

Bisaria D., Spekkens K., Huang S., Hallenbeck G., Haynes M. P., 2022, *MNRAS*, **509**, 100

Blumenthal G. R., Faber S. M., Flores R., Primack J. R., 1986, *ApJ*, **301**, 27

Bosma A., 1981, *AJ*, **86**, 1825

Boubel P., Colless M., Said K., Staveley-Smith L., 2024, *MNRAS*, **533**, 1550

Bouché N., Carfantan H., Schroetter I., Michel-Dansac L., Contini T., 2015, *AJ*, **150**, 92

Bouché N. F., et al., 2021, *A&A*, **654**, A49

Bouché N. F., et al., 2022, *A&A*, **658**, A76

Bullock J. S., Kolatt T. S., Sigad Y., Somerville R. S., Kravtsov A. V., Klypin A. A., Primack J. R., Dekel A., 2001, *MNRAS*, **321**, 559

Bundy K., et al., 2015, *ApJ*, **798**, 7

Burbidge E. M., Burbidge G. R., Prendergast K. H., 1959, *ApJ*, **130**, 26

Burkert A., 2015, *ApJ*, **808**, 158

Burkert A., et al., 2010a, *Astrophysical Journal*, **725**, 2324

Burkert A., et al., 2010b, *ApJ*, **725**, 2324

Burkert A., et al., 2016, *ApJ*, **826**, 214

Cappellari M., et al., 2013, *MNRAS*, **432**, 1709

Chen C.-C., et al., 2017, *ApJ*, **846**, 108

Chugunov I. V., Marchuk A. A., Mosenkov A. V., 2025, *Publ. Astron. Soc. Australia*, **42**, e029

Ciocan B. I., Ziegler B. L., Böhm A., Verdugo M., Maier C., 2022, *A&A*, **667**, A61

Ciotti L., Bertin G., 1999, *A&A*, **352**, 447

Contini T., et al., 2016, *A&A*, **591**, A49

Courteau S., 1997, *AJ*, **114**, 2402

Courteau S., Dutton A. A., 2015, *ApJ*, **801**, L20

Cresci G., et al., 2009, *ApJ*, **697**, 115

Croom S. M., et al., 2021, *MNRAS*, **505**, 991

Danhaine A. L., et al., 2025a, *arXiv e-prints*, p. arXiv:2510.14779

Danhaine A. L., et al., 2025b, *MNRAS*, **543**, 3249

Davies R. I., Tacconi L. J., Genzel R., 2004a, *ApJ*, **602**, 148

Davies R. I., Tacconi L. J., Genzel R., 2004b, *ApJ*, **613**, 781

Davies R., et al., 2011, *Astrophysical Journal*, **741**, 69

Deg N., et al., 2022, *Publ. Astron. Soc. Australia*, **39**, e059

Dekel A., Mandelker N., Bournaud F., Ceverino D., Guo Y., Primack J., 2022, *MNRAS*, **511**, 316

Di Folco E., Péricaud J., Dutrey A., Augereau J.-C., Chapillon E., Guilloteau S., Piétu V., Boccaletti A., 2020, *A&A*, **635**, A94

Di Teodoro E. M., Fraternali F., 2015, *MNRAS*, **451**, 3021

Di Teodoro E. M., Fraternali F., Miller S. H., 2016, *A&A*, **594**, A77

Di Teodoro E. M., Posti L., Ogle P. M., Fall S. M., Jarrett T., 2021, *MNRAS*, **507**, 5820

Di Teodoro E. M., et al., 2023, *MNRAS*, **518**, 6340

Dutton A. A., Macciò A. V., 2014, *MNRAS*, **441**, 3359

Einasto J., 1965, Trudy Astrofizicheskogo Instituta Alma-Ata, **5**, 87

Elagali A., Wong O. I., Oh S.-H., Staveley-Smith L., Koribalski B. S., Bekki K., Zwaan M., 2018, *MNRAS*, **476**, 5681

Epinat B., et al., 2009, *A&A*, **504**, 789

Espejo Salcedo J. M., Glazebrook K., Fisher D. B., Sweet S. M., Obreschkow D., Schreiber N. M. F., 2025a, *MNRAS*, **536**, 1188

Espejo Salcedo J. M., et al., 2025b, *A&A*, **700**, A42

Fei Q., et al., 2025, *ApJ*, **980**, 84

Ferreira L., et al., 2023, *ApJ*, **955**, 94

Foreman-Mackey D., 2016, *The Journal of Open Source Software*, **1**, 24

Foreman-Mackey D., Hogg D. W., Lang D., Goodman J., 2013b, *Publications of the Astronomical Society of the Pacific*, **125**, 306

Foreman-Mackey D., Hogg D. W., Lang D., Goodman J., 2013a, *PASP*, **125**, 306

Förster Schreiber N. M., Wuyts S., 2020, *ARA&A*, **58**, 661

Förster Schreiber N. M., et al., 2009, *ApJ*, **706**, 1364

Förster Schreiber N. M., et al., 2018, *ApJS*, **238**, 21

Freedman W. L., et al., 2001, *ApJ*, **553**, 47

Freundlich J., et al., 2020, *MNRAS*, **499**, 2912

Fujimoto S., et al., 2025, *Nature Astronomy*,

Genzel R., et al., 2006, *Nature*, **442**, 786

Genzel R., et al., 2011, *ApJ*, **733**, 101

Genzel R., et al., 2013, *ApJ*, **773**, 68

Genzel R., et al., 2017, *Nature*, **543**, 397

Genzel R., et al., 2020, *ApJ*, **902**, 98

Genzel R., et al., 2023, *ApJ*, **957**, 48

Géron T., et al., 2025, *ApJ*, **987**, 74

Girard M., et al., 2021, *ApJ*, **909**, 12

Gnerucci A., et al., 2011, *A&A*, **528**, A88

Gómez-López J. A., et al., 2019, *A&A*, **631**, A71

Governato F., et al., 2012, *MNRAS*, **422**, 1231

Guérou A., et al., 2017, *A&A*, **608**, A5

Gunn J. E., 1980, *Philosophical Transactions of the Royal Society of London Series A*, **296**, 313

Hamilton-Campos K. A., Simons R. C., Peebles M. S., Snyder G. F., Heckman T. M., 2023, *ApJ*, **956**, 147

Harrison C. M., et al., 2017, *MNRAS*, **467**, 1965

Herrera-Camus R., et al., 2022, *A&A*, **665**, L8

Herrera-Camus R., et al., 2025, *A&A*, **699**, A80

Huertas-Company M., et al., 2024, *A&A*, **685**, A48

Hunter J. D., 2007, *Computing in Science and Engineering*, **9**, 90

Hunter D. A., et al., 2012, *AJ*, **144**, 134

Iorio G., Fraternali F., Nipoti C., Di Teodoro E., Read J. I., Battaglia G., 2017, *MNRAS*, **466**, 4159

Jones G. C., et al., 2021, *MNRAS*, **507**, 3540

Jones G. C., et al., 2025, *arXiv e-prints*, p. arXiv:2512.05213

Kartaltepe J. S., et al., 2023, *ApJ*, **946**, L15

Kim S., Oh S.-H., For B.-Q., Sheen Y.-K., 2020, *The Bulletin of The Korean Astronomical Society*, **45**, 60.3

Kuhn V., Guo Y., Martin A., Bayless J., Gates E., Puleo A., 2024, *ApJ*, **968**, L15

Kuzio de Naray R., Arsenault C. A., Spekkens K., Sellwood J. A., McDonald M., Simon J. D., Teuben P., 2012, DiskFit: Modeling Asymmetries in Disk Galaxies, Astrophysics Source Code Library, record ascl:1209.011 (ascl:1209.011)

Lang P., et al., 2017, *ApJ*, **840**, 92

Lang P., et al., 2020, *ApJ*, **897**, 122

Law D. R., Steidel C. C., Erb D. K., Larkin J. E., Pettini M., Shapley A. E., Wright S. A., 2009, *ApJ*, **697**, 2057

Lazar A., et al., 2020, *MNRAS*, **497**, 2393

Lee L. L., et al., 2025a, *A&A*, **701**, A260

Lee L. L., et al., 2025b, *ApJ*, **978**, 14

Leethochawalit N., Jones T. A., Ellis R. S., Stark D. P., Richard J., Zitrin A., Auger M., 2016, *ApJ*, **820**, 84

Lelli F., McGaugh S. S., Schombert J. M., 2016a, *AJ*, **152**, 157

Lelli F., McGaugh S. S., Schombert J. M., 2016b, *ApJ*, **816**, L14

Lelli F., McGaugh S. S., Schombert J. M., Pawlowski M. S., 2017, *ApJ*, **836**, 152

Lelli F., McGaugh S. S., Schombert J. M., Desmond H., Katz H., 2019, *MNRAS*, **484**, 3267

Lian J., Luo L., 2024, *ApJ*, **960**, L10

Liu D., et al., 2023a, *ApJ*, **942**, 98

Liu D., et al., 2023b, *ApJ*, **942**, 98

Liu J., Li Z., Shen J., 2025, *ApJ*, **980**, 146

Livermore R. C., et al., 2015, *MNRAS*, **450**, 1812

Mancini C., et al., 2011, *ApJ*, **743**, 86

Marconcini C., et al., 2024, *MNRAS*, **533**, 2488

Martinsson T. P. K., Verheijen M. A. W., Westfall K. B., Bershady M. A., Andersen D. R., Swaters R. A., 2013, [A&A](#), **557**, A131

Mason C. A., et al., 2017, [ApJ](#), **838**, 14

McGaugh S. S., Schombert J. M., Bothun G. D., de Blok W. J. G., 2000, [ApJ](#), **533**, L99

Mo H. J., Mao S., White S. D. M., 1998, [MNRAS](#), **295**, 319

Molina J., Ibar E., Smail I., Swinbank A. M., Villard E., Escala A., Sobral D., Hughes T. M., 2019, [MNRAS](#), **487**, 4856

Moster B. P., Naab T., White S. D. M., 2018, [MNRAS](#), **477**, 1822

Navarro J. F., Frenk C. S., White S. D. M., 1996, [Astrophysical Journal](#), **462**, 563

Navarro J. F., Frenk C. S., White S. D. M., 1997, [ApJ](#), **490**, 493

Navarro J. F., et al., 2004, [MNRAS](#), **349**, 1039

Nestor Shachar A., et al., 2023, [ApJ](#), **944**, 78

Nestor Shachar A., et al., 2025, [ApJ](#), **988**, 182

Noordermeer E., 2008, [Monthly Notices of the Royal Astronomical Society](#), **385**, 1359

Oh S.-H., Wang J., 2025, [MNRAS](#), **538**, 1816

Oh S.-H., de Blok W. J. G., Brinks E., Walter F., Kennicutt Jr. R. C., 2011, [AJ](#), **141**, 193

Oh S.-H., et al., 2015, [AJ](#), **149**, 180

Oh S.-H., Staveley-Smith L., Spekkens K., Kamphuis P., Koribalski B. S., 2018, [MNRAS](#), **473**, 3256

Oh S.-H., Staveley-Smith L., Spekkens K., Kamphuis P., Koribalski B. S., 2020, 2DBAT: 2D Bayesian Automated Tilted-ring fitter, [Astrophysics Source Code Library](#), record ascl:2005.012 (ascl:2005.012)

Oh S.-H., Kim S., For B.-Q., Staveley-Smith L., 2022, [ApJ](#), **928**, 177

Oh S.-H., Kim S., Kim S.-J., Koribalski B. S., 2025, [Ap&SS](#), **370**, 129

Pastras S., et al., 2025, [arXiv e-prints](#), p. arXiv:2505.07925

Posses A., et al., 2024, [arXiv e-prints](#), p. arXiv:2403.03379

Price S. H., et al., 2021, [ApJ](#), **922**, 143

Price S. H., et al., 2022, [A&A](#), **665**, A159

Puglisi A., et al., 2023, [MNRAS](#), **524**, 2814

Read J. I., Walker M. G., Steger P., 2019, [MNRAS](#), **484**, 1401

Richards E. E., et al., 2016, [MNRAS](#), **460**, 689

Rizzo F., Vegetti S., Fraternali F., Stacey H. R., Powell D., 2021, [MNRAS](#), **507**, 3952

Rizzo F., et al., 2023, [A&A](#), **679**, A129

Rizzo F., et al., 2024, [A&A](#), **689**, A273

Roman-Oliveira F., Rizzo F., Fraternali F., 2024, [A&A](#), **687**, A35

Romeo A. B., Burkert A., Agertz O., 2010, [MNRAS](#), **407**, 1223

Rowland L. E., et al., 2024, [MNRAS](#), **535**, 2068

Rubin V. C., Ford Jr. W. K., 1970, [ApJ](#), **159**, 379

Sánchez S. F., et al., 2016, [A&A](#), **594**, A36

Sánchez S. F., Galbany L., Walcher C. J., García-Benito R., Barrera-Ballesteros J. K., 2023, [MNRAS](#), **526**, 5555

Schaye J., et al., 2015, [MNRAS](#), **446**, 521

Scholtz J., et al., 2025, [arXiv e-prints](#), p. arXiv:2503.10751

Schombert J., McGaugh S., Lelli F., 2020, [AJ](#), **160**, 71

Sellwood J. A., Spekkens K., 2015, [arXiv e-prints](#), p. arXiv:1509.07120

Smethurst R. J., et al., 2025, [MNRAS](#), **539**, 1359

Smit R., et al., 2018, [Nature](#), **553**, 178

Somerville R. S., Davé R., 2015, [ARA&A](#), **53**, 51

Spitzer Jr. L., 1942, [ApJ](#), **95**, 329

Stott J. P., et al., 2016, [MNRAS](#), **457**, 1888

Szakacs R., et al., 2021, [MNRAS](#), **505**, 4746

Tacconi L. J., et al., 2013, [ApJ](#), **768**, 74

Tacconi L. J., et al., 2018, [ApJ](#), **853**, 179

Tadaki K., et al., 2018, [Nature](#), **560**, 613

Telikova K., et al., 2025, [A&A](#), **699**, A5

The pandas development Team 2024, pandas-dev/pandas: Pandas, [doi:10.5281/zenodo.3509134](https://doi.org/10.5281/zenodo.3509134)

Tiley A. L., et al., 2019, [MNRAS](#), **485**, 934

Tiley A. L., et al., 2021, [MNRAS](#), **506**, 323

Tohill C., Bamford S. P., Conselice C. J., Ferreira L., Harvey T., Adams N., Austin D., 2024, [ApJ](#), **962**, 164

Toomre A., 1964, [The Astrophysical Journal](#), **139**, 1217

Tsukui T., Wisnioski E., Bland-Hawthorn J., Freeman K., 2025, [MNRAS](#), **540**, 3493

Tully R. B., Fisher J. R., 1977, [A&A](#), **54**, 661

Übler H., et al., 2017, [ApJ](#), **842**, 121

Übler H., et al., 2018, [ApJ](#), **854**, L24

Übler H., et al., 2019, [ApJ](#), **880**, 48

Übler H., et al., 2024a, [MNRAS](#), **527**, 9206

Übler H., et al., 2024b, [MNRAS](#), **533**, 4287

Virtanen P., et al., 2020, [Nature Methods](#), **17**, 261

Vogelsberger M., et al., 2014, [MNRAS](#), **444**, 1518

Walter F., Brinks E., de Blok W. J. G., Bigiel F., Kennicutt Jr. R. C., Thornley M. D., Leroy A., 2008, [AJ](#), **136**, 2563

Waskom M. L., 2021, [Journal of Open Source Software](#), **6**, 3021

Westmeier T., et al., 2022, [Publ. Astron. Soc. Australia](#), **39**, e058

Wisnioski E., et al., 2015, [ApJ](#), **799**, 209

Wisnioski E., et al., 2019, [ApJ](#), **886**, 124

Wisnioski E., Mendel J. T., Leaman R., Tsukui T., Übler H., Schreiber N. M. F., 2025, [MNRAS](#),

Wong O. I., et al., 2021, [MNRAS](#), **507**, 2905

Wuyts S., et al., 2016, [ApJ](#), **831**, 149

Yoon Y., Park C., Chung H., Zhang K., 2021, [ApJ](#), **922**, 249

Yttergren M., Knudsen K. K., Molina J., Jones G. C., Kade K., Scholtz J., Bewketu Belete A., 2025, [MNRAS](#), **543**, 3103

Zhang H.-X., et al., 2020, [ApJ](#), **900**, 152

Zhao H., 1996, [MNRAS](#), **278**, 488

de Blok W. J. G., 2010, [Advances in Astronomy](#), **2010**, 789293

de Blok W. J. G., Walter F., Brinks E., Trachternach C., Oh S. H., Kennicutt Jr. R. C., 2008, [AJ](#), **136**, 2648

de Graaff A., et al., 2024a, [A&A](#), **684**, A87

de Graaff A., et al., 2024b, [A&A](#), **684**, A87

van Albada T. S., Sancisi R., 1986, [Philosophical Transactions of the Royal Society of London Series A](#), **320**, 447

van Albada T. S., Bahcall J. N., Begeman K., Sancisi R., 1985, [ApJ](#), **295**, 305

van der Kruit P. C., Allen R. J., 1978, [ARA&A](#), **16**, 103

van der Walt S., Colbert S. C., Varoquaux G., 2011, [Computing in Science and Engineering](#), **13**, 22

van der Wel A., Meidt S. E., 2025, [arXiv e-prints](#), p. arXiv:2509.02847

This paper has been typeset from a  $\text{\TeX}$ / $\text{\LaTeX}$  file prepared by the author.